INFORMATION TO USERS

This manuscript has been reproduced from the microfilm master. UMI films the text directly from the original or copy submitted. Thus, some thesis and dissertation copies are in typewriter face, while others may be from any type of computer printer.

The quality of this reproduction is dependent upon the quality of the copy submitted. Broken or indistinct print, colored or poor quality illustrations and photographs, print bleedthrough, substandard margins, and improper alignment can adversely affect reproduction.

In the unlikely event that the author did not send UMI a complete manuscript and there are missing pages, these will be noted. Also, if unauthorized copyright material had to be removed, a note will indicate the deletion.

Oversize materials (e.g., maps, drawings, charts) are reproduced by sectioning the original, beginning at the upper left-hand corner and continuing from left to right in equal sections with small overlaps. Each original is also photographed in one exposure and is included in reduced form at the back of the book.

Photographs included in the original manuscript have been reproduced xerographically in this copy. Higher quality 6" x 9" black and white photographic prints are available for any photographs or illustrations appearing in this copy for an additional charge. Contact UMI directly to order.

UMI

A Bell & Howell Information Company
300 North Zeeb Road, Ann Arbor MI 48106-1346 USA
313/761-4700 800/521-0600

Reproduced with permission of the copyright owner. Further reproduction prohibited without permission.

Reproduced with permission of the copyright owner. Further reproduction prohibited without permission.

EXPERIMENTAL OPTICAL-SPECTROSCOPY STUDY OF:

a) The liquid-glass transition in glycerol. A mode coupling theory analysis.
b) Low-frequency light scattering from powders. Multiple scattering model.
c) Side chain intramolecular hydrogen - bond interactions in helical peptides.

by

Joel Hernandez

A dissertation submitted to the Graduate Faculty in Physics in partial fulfillment of the requirements for the degree of Doctor of Philosophy

The City University of New York

1997

Reproduced with permission of the copyright owner. Further reproduction prohibited without permission.

UMI Number: 9807939

UMI Microform 9807939
Copyright 1997, by UMI Company. All rights reserved.

This microform edition is protected against unauthorized copying under Title 17, United States Code.

UMI
300 North Zeeb Road
Ann Arbor, MI 48103

Reproduced with permission of the copyright owner. Further reproduction prohibited without permission.

This manuscript has been read and accepted for the Graduate Faculty in Physics in satisfaction of the dissertation requirement for the degree of Doctor of Philosophy.

5/13/1997 — Date — Chair of Examining Committee

5/13/97 — Date — Executive Officer

Joseph L. Birman
Steven G. Greenbaum
Frederick W. Smith
Robert H. Callender

Supervisory Committee

The City University of New York

Reproduced with permission of the copyright owner. Further reproduction prohibited without permission.

Abstract

EXPERIMENTAL OPTICAL-SPECTROSCOPY STUDY OF:

a) The liquid-glass transition in glycerol. A mode coupling theory analysis.
b) Low-frequency light scattering from powders. Multiple scattering model.
c) Side chain intramolecular hydrogen - bond interactions in helical peptides.

by

Joel Hernandez

Advisers: Professors Herman Z. Cummins and Robert Callender

Depolarized light-scattering spectra of the intermediate glass-former glycerol were obtained in the frequency and temperature ranges of 0.4 to 6000 GHz and 173 to 413 K respectively. Analysis of the resulting susceptibility spectra using the asymptotic leading order equations of mode coupling theory (MCT) showed only partial agreement between theory and experiment. However, a recent analysis of our data using a full numerical solution of the MCT equations has been remarkably successful, widening the applicability of the theory to weak network glass-formers and motivating the need to conduct similar tests with strong network glass-formers.

The accidental discovery of a low-frequency band in the light scattering spectrum from a powder of the protein lysozyme lead us to the development of a model for that kind of scattering. Such a model was found to be in very good agreement with our experimental data.

A preliminary infrared absorption experiment on synthesized helical peptides, containing glutamic acid (Glu) amino acid residues spaced periodically along the

Reproduced with permission of the copyright owner. Further reproduction prohibited without permission.

polypeptide chain, showed evidence for the stabilization of the helical structure of the peptide, by intramolecular hydrogen bonding interactions between the carboxylic acid groups in the side chains of the Glu residues.

Reproduced with permission of the copyright owner. Further reproduction prohibited without permission.

TABLE OF CONTENTS

Reproduced with permission of the copyright owner. Further reproduction prohibited without permission.

Reproduced with permission of the copyright owner. Further reproduction prohibited without permission.

ACKNOWLEDGMENTS

I owe special gratitude to my advisers Distinguished Professors Herman Z. Cummins and Robert Callender for their constant education, guidance and financial support during my research at City College.

I am very grateful to Dr. Myer M. Fishman as director of the minority research programs in City College for providing a major part of my financial support and for allowing my participation in many national and international research conferences.

I thank Professor Robert M. Pick for his suggestions during the development of the model for the low frequency light scattering from powders.

I sincerely thank the other members of my examining committee, Professors Joseph L. Birman, Frederick W. Smith and Steven G. Greenbaum, for their productive discussions and suggestions.

I very much thank Drs. Gen Li and Rudolf Gilmanshin for the valuable practical training received from them during my experimental work.

I thank my other co-workers Dr.Yoon-Hwae Hwang, Guoqing P. Shen, Wolfgang Losert, Hui Zhung, Dr. Zhongmo Ju, Jianghua Wang, Dr. Weimin Du, Dr. Dongning Liu, Dr. Bill Shi, Dr. Lloyd Williams, and Dr. Martin Muschol for their friendship.

Many thanks to Tracy Turner, Naomi Hellmann and Sonia Mathew for their secretarial services.

Finally, thanks to all my former professors, and family for their encouragement to initiate and complete this work.

Reproduced with permission of the copyright owner. Further reproduction prohibited without permission.

LIST OF TABLES

LIST OF FIGURES

Reproduced with permission of the copyright owner. Further reproduction prohibited without permission.

1. INTRODUCTION

This thesis is devoted primarily to the experimental analysis of the validity of the Mode Coupling Theory (MCT) for the liquid to glass transition in an intermediate glass former like glycerol. Mode coupling methods were introduced initially by Kawasaki [1] to study critical phenomena. In 1984 it was used for the first time to study the liquid to glass transition [2, 3]. The theory was intended for fragile glass formers and several experimental tests corroborated its validity [4, 5, 6, 7, 8, 9, 10, 11 and 12] in these systems. However, its applicability for network forming materials was uncertain because the theory didn't have any provision for the dynamics of bond breaking and formation. We were interested in testing its validity with the weak network glass former glycerol. The comparison of our data with the asymptotic leading order equations of the theory showed only partial agreement. These results supported the belief that MCT was not valid for network glass formers. However, a recent analysis using a full numerical solution of the MCT equations showed a remarkable good agreement with our data. This last result showed that the MCT for the liquid to glass transition addresses the most relevant processes for the dynamics of glass forming materials.

The rest of the thesis contains two other results that derived from research of a biophysical nature. These are the low frequency light scattering from powders and the study of conformational changes in peptides.

During the search for very low frequency vibrations in proteins, specifically, the hinge-bending mode in lysozyme, a low frequency band was discovered in the

Reproduced with permission of the copyright owner. Further reproduction prohibited without permission.

spectrum of a lyophilized powder of lysozyme. The band, (initially suspected to be related to the looked for mode) was subsequently observed in the spectrum from any powder; it was found to be the result of Brillouin scattering from all scattering angles due to multiple elastic scattering of light in the sample. This band had not previously been reported, probably due to the fact that it is very weak and appears in the presence of a very strong elastic scattering line. We developed a theoretical model for Brillouin scattering from powders of isotropic materials and compared it successfully with our experiments.

The final section, the analysis of conformational changes in peptides, is a preliminary work intended to corroborate the possibility of stabilization of the helical structure in man-made peptides containing glutamic acid residues spaced periodically. This stabilization is supposed to take place due to H-bond interactions via the carboxylic acid group in the side chains of glutamic acid residues. Our infrared absorption measurements as a function of pH showed correlation between the pKa shift of the peptide (with respect to the isolated glutamic acid) and the change in the helical content of the peptides. This result suggests the possibility of such a stabilization mechanism.

Reproduced with permission of the copyright owner. Further reproduction prohibited without permission.

2. LIGHT SCATTERING THEORY AND EXPERIMENTAL TECHNIQUES

2.1 Correlation functions, power spectra and linear response function

The time correlation function of a quantity A(t) is defined by

$$C^{A}(t) \equiv \left\langle A^{*}(0)\ A(t) \right\rangle = \lim_{T\to\infty} \frac{1}{T} \int_{0}^{T} dt'\ A(t')\ A(t'+t) \qquad (2.1.1)$$

$C^{A}(t)$ is a measure of the correlation between the values of A at times t' and (t' + t) averaged over t' . The Fourier transform of $C^{A}(t)$ gives the power spectrum $I^{A}(\omega)$.

$$I^{A}(\omega) \equiv \frac{1}{2\pi} \int_{-\infty}^{\infty} dt\, e^{-i\omega t} C^{A}(t) \qquad (2.1.2)$$

Similarly, $C^{A}(t)$ can be obtained from $I^{A}(\omega)$ via the inverse Fourier transform.

$$C^{A}(t) \equiv \int_{-\infty}^{\infty} d\omega\, e^{i\omega t} I^{A}(\omega) \qquad (2.1.3)$$

Evaluating Eq.(2.1.3) for t = 0 gives

Reproduced with permission of the copyright owner. Further reproduction prohibited without permission.

$$C^{A}(0) = \left\langle \left| A(0) \right|^{2} \right\rangle = \int_{-\infty}^{\infty} d\omega \, I^{A}(\omega) \equiv I^{A} \qquad (2.1.4)$$

From Eq.(2.1.4) we see that the integrated power I^{A} can be obtained not only by direct integration of $I^{A}(\omega)$ but also by evaluation of $C^{A}(t)$ at t=0.

Consider now that the property A couples to a conjugate field a. Then, in the linear response regime, the deviation of A from its average is proportional to the conjugate field

$$\delta A(\mathbf{q}, \omega) = \chi(\mathbf{q}, \omega)\, a(\omega) \qquad (2.1.5)$$

$\chi(q, \omega)$ is called the linear response function (or susceptibility) for the variable A. An example is the dielectric susceptibility which relates the polarization **P** induced in a medium to the electric field **E**. Then, the quantities in Eq. (2.1.5) correspond to

$$\delta A(\mathbf{q}, \omega) = \delta \mathbf{P}(\mathbf{q}, \omega),$$

$$a(\omega) = \mathbf{E}(\omega)$$

and $\chi(\mathbf{q}, \omega)$ is the dynamic dielectric polarizability, related to the dielectric constant by

$$\varepsilon(\mathbf{q}, \omega) = 1 + 4\pi \chi(\mathbf{q}, \omega)$$

Reproduced with permission of the copyright owner. Further reproduction prohibited without permission.

$\chi(q, \omega)$ is a complex function. The imaginary part $\chi''(q, \omega)$ is related to the light scattering spectrum as will be explained in section 2.5.

Reproduced with permission of the copyright owner. Further reproduction prohibited without permission.

2.2 Macroscopic approach to light scattering.[13]

Classically, the principal origin of low-frequency inelastic scattering of light from a continuous medium is mass density fluctuations which produce fluctuations in the local dielectric constant and polarization of the medium. Consider a non-magnetic, non-conducting, non-absorbing medium with average (ε_o) and fluctuating ($\delta\varepsilon$) parts for the dielectric constant tensor.

$$\boldsymbol{\varepsilon}(\mathbf{r}, t) = \varepsilon_0 \mathbf{I} + \delta\boldsymbol{\varepsilon}(\mathbf{r}, t) \tag{2.2.1}$$

Let the incident electric field be a plane wave of the form

$$\mathbf{E}_o(\mathbf{r}, t) = \mathbf{n}_o E_0 e^{i(\mathbf{k}_o \cdot \mathbf{r} - \omega_o t)} \tag{2.2.2}$$

where $\mathbf{n}_o$ is the unit polarization vector, E_o the amplitude, $\mathbf{k}_o$ the wavevector and ω_o the angular frequency. When light passes through the medium, there will be an excess polarization $\delta\mathbf{P}$ related to the excess dielectric constant $\delta\boldsymbol{\varepsilon}$ and the scattered field can be calculated from this excess polarization. Calculation of the spectrum of the scattered light gives [13]

$$I^E_{\alpha\beta}(q,\omega_s) \;\alpha\; \frac{1}{2\pi}\int_{-\infty}^{\infty} dt\, e^{i(\omega_s-\omega_o)t}\left\langle \delta^* \varepsilon_{\alpha\beta}(q,0)\,\delta\varepsilon_{\alpha\beta}(q,t)\right\rangle \tag{2.2.3}$$

Reproduced with permission of the copyright owner. Further reproduction prohibited without permission.

where **q** is the wavevector of the dielectric constant fluctuations, ω_s the angular frequency of the scattered light, and $\delta\varepsilon_{os}(\mathbf{q}, t) \equiv \mathbf{n}_s \,.\, \delta\varepsilon(\mathbf{q}, t) \,.\, \mathbf{n}_o$ is the component of the dielectric constant fluctuation tensor along the incident ($\mathbf{n}_o$) and scattered ($\mathbf{n}_s$) polarization directions. Also, $\delta\varepsilon(\mathbf{q}, t)$ is the space Fourier transform of $\delta\varepsilon(\mathbf{r}, t)$.

$$\delta\varepsilon(\mathbf{q}, t) = \int_V d^3 r\, e^{i\mathbf{q}\cdot\mathbf{r}}\, \delta\varepsilon\ (r,t) \qquad (2.2.4)$$

Eq. (2.2.3) is very informative. Consider the following three different situations:

I- **Frozen, homogeneous medium:** In this case $\delta\varepsilon_{os}(\mathbf{r}, t)$ is zero and so is the scattering intensity. Strictly speaking, there would be elastic scattering ($\omega_s = \omega_o$) in the forward (q=0) direction only. Forward scattering can be derived from a microscopic theory of light scattering and this is beyond our intentions here.

II-**Frozen, inhomogeneous medium**: In this case $\delta\varepsilon_{os}(\mathbf{r}, t) = \delta\varepsilon_{os}\ (\mathbf{r}, 0)$ and the spectrum is

$$I(q,\omega_s) \propto \left\langle \left|\delta\varepsilon_{os}(q,0)\right|^2 \right\rangle \frac{1}{2\pi} \int_{-\infty}^{\infty} dt\, e^{i(\omega_s-\omega_o)t} = \left\langle \left|\delta\varepsilon_{os}(q,0)\right|^2 \right\rangle \delta(\omega_s-\omega_o)$$

Reproduced with permission of the copyright owner. Further reproduction prohibited without permission.

Thus, the spectrum will again consist of elastic scattering but now it is not restricted to the forward direction. This scattering will produce a static speckle pattern on a screen.

III-**Unfrozen, inhomogeneous medium**: In this case Eq. (2.2.3) does not lead to any Dirac delta function. Thus, scattering is not restricted either to elastic type or to the forward direction. This will produce a dynamic speckle pattern.

The excess dielectric constant can be Taylor expanded in terms of the density and temperature fluctuations. Commonly, the variations of the dielectric constant tensor due to temperature fluctuations is very small, compared to the variations due to density fluctuations; therefore, temperature fluctuations are usually neglected in the expansion. Under these conditions, the expansion will look

$$\varepsilon(q,\omega) = \frac{\partial \varepsilon}{\partial \rho}\delta\rho_q + \frac{\partial^2 \varepsilon}{\partial \rho^2}\delta\rho_{q_1}\delta\rho_{q_2} + \cdots \qquad (2.2.5)$$

Linear (or first order) scattering refers to scattering due to the linear term, second order scattering refers to the second term and so on. Shear strains, while not causing density fluctuations, nevertheless perturb off-diagonal components of the dielectric tensor and cause depolarized light scattering.

Reproduced with permission of the copyright owner. Further reproduction prohibited without permission.

2.3 Molecular approach to light scattering.[13]

In addition to the macroscopic formulation just described in terms of the dielectric constant tensor, it is possible to follow a molecular approach based on the molecular polarizability tensor as follows.

If an incident monochromatic beam as in Eq. (2.2.2) interacts with a molecule characterized by its polarizability tensor α, a time varying dipole moment $\mu(t) = \alpha.E(t)$ is induced and the oscillating dipole then emits electromagnetic radiation. If the molecules in the scattering volume are electronically weakly coupled, that is, if the electronic states of the molecules are not perturbed very much by their neighbors, the total scattered field will be given by the superposition of the electric field originating from each molecule independently. The spectrum of the scattered field is found to be proportional to the power spectrum of the polarizability fluctuations $\delta\alpha$.

$$I^{E}_{\alpha s}(q,\omega) \quad \alpha \; I^{\alpha}_{\alpha s}(q,\omega) \equiv \frac{1}{2\pi}\int_{-\infty}^{\infty} dt\, e^{-i\omega t} C^{\alpha}_{\alpha s}(q,t) \tag{2.3.1}$$

where

$$C^{\alpha}_{\alpha s}(q,t) \equiv \left\langle \delta\alpha^{*}_{\alpha s}(q,0)\delta\alpha_{\alpha s}(q,t)\right\rangle , \tag{2.3.2}$$

$$\delta\alpha_{\alpha s}(q,t) = \sum_{j=1}^{N} \alpha^{j}_{\alpha s}(t) e^{iq\cdot r_j(t)}, \tag{2.3.3}$$

Reproduced with permission of the copyright owner. Further reproduction prohibited without permission.

and

$$\alpha^{j}_{os}(t) = n_s \cdot \alpha^{j}(t) \cdot n_o \quad , \tag{2.3.4}$$

and N is the number of molecules in the scattering volume. Observe that the fluctuations $\delta\alpha_{os}(q,t)$ in Eq. (2.3.3) originate due to translations (via $r_j(t)$) and rotations (via $\alpha^{j}_{os}(t)$) of the molecule.

The usefulness of this approach can be illustrated by considering the scattering from a system of isotropic molecules for which the polarizability tensor is just a scalar α. Then Eqs. (2.3.2-4) become:

$$\alpha_{os}(t) = (\mathbf{n}_o \cdot \mathbf{n}_s) \, \alpha \, ,$$

$$\alpha_{os}(q,t) = (n_o \cdot n_s) \, \alpha \sum_{j=1}^{N} e^{i q \cdot r_j(t)} ,$$

$$C^{\alpha}_{os}(q,t) = (n_o \cdot n_s)^2 \, \alpha^2 \left\langle \left(\sum_{j=1}^{N} e^{-q \cdot r_j(0)} \right) \left(\sum_{i=1}^{N} e^{q \cdot r_i(t)} \right) \right\rangle$$

If the system is dilute, we can consider to a first approximation that the positions of different molecules are statistically independent. Then the correlation function reduces to

Reproduced with permission of the copyright owner. Further reproduction prohibited without permission.

$$C_{\alpha\alpha}^{\alpha}(q,t) = \left(n_O.n_S\right)^2 \alpha^2 \langle N \rangle F_s(q,t) \qquad (2.3.5)$$

where the function $F_s(q, t)$ (called the self-intermediate scattering function) is:

$$F_s(q,t) = \left\langle e^{iq\left(r_j(t)-r_j(0)\right)} \right\rangle \qquad (2.3.6)$$

Calculation of F_s requires the assumption of some dynamical model for the translational motion of the molecules like diffusive or free motion. In the case of translational diffusion, F_s is given by

$$F_s(q,t) = e^{-q^2 D t} \qquad (2.3.7)$$

where D is the coefficient of self-diffusion of the molecules. This simple exponential decay is commonly called Debye or Maxwell relaxation since they used it to describe electric dipole and viscoelastic relaxation respectively.

For incident light polarized perpendicular to the scattering plane (V) and scattered light polarized parallel (H) or perpendicular (V) to the scattering plane, the dot product of the unit vectors in Eq. (2.3.5) gives $\mathbf{n}_V.\mathbf{n}_V = 1$ and $\mathbf{n}_V.\mathbf{n}_H = 0$ respectively. Then, for the translational diffusion case, from Eqs.(2.3.5) and (2.3.7) we get:

Reproduced with permission of the copyright owner. Further reproduction prohibited without permission.

$$C^{\alpha}_{VV}(q,t) = \alpha^2 \langle N \rangle e^{-q^2 D t} \tag{2.3.8a}$$

and

$$C^{\alpha}_{VH}(q,t) = 0 \tag{2.3.8b}$$

Thus, isotropic molecules do not produce depolarized (VH) scattering. This last result is strictly true only for non-interacting particles as will be explained in section 2.4b.

To finish the illustration of the molecular approach we can consider briefly the case of anisotropic molecules. In this case, we can not simplify $\alpha_{\alpha s}(t)$ as we did for isotropic molecules. From Eqs. (2.3.2,3), the explicit form for the correlation function of the polarizability fluctuations is:

$$C^{\alpha}_{\alpha s}(q,t) \equiv \left\langle \delta\alpha^{*}_{\alpha s}(q,0)\,\delta\alpha_{\alpha s}(q,t) \right\rangle = \left\langle \left(\sum_{j=1}^{N} \alpha^{j}_{\alpha s}(0) e^{-i q \cdot r_j(0)} \right) \left(\sum_{l=1}^{N} \alpha^{l}_{\alpha s}(t) e^{i q \cdot r_l(t)} \right) \right\rangle \tag{2.3.9}$$

If the position of the molecules are statistically independent, this simplifies to

$$C^{\alpha}_{\alpha s}(q,t) = \left\langle \left(\sum_{j=1}^{N} \alpha^{j}_{\alpha s}(0) \alpha^{j}_{\alpha s}(t) e^{i q \cdot (r_j(t) - r_j(0))} \right) \right\rangle \tag{2.3.10}$$

Reproduced with permission of the copyright owner. Further reproduction prohibited without permission.

If the position and orientation of a molecule are statistically independent (decoupling of rotations and translations), the expression reduces further to

$$C^{\alpha}_{\alpha\alpha}(q,t) = \langle N \rangle \langle \alpha_{\alpha\alpha}(0)\alpha_{\alpha\alpha}(t) \rangle F_s(q,t) \qquad (2.3.11)$$

where F_s was defined above in Eq. (2.3.6). Thus, in this anisotropic case the correlation function has two decay channels; one is associated with translational motion (F_s) and the other with rotations ($< \alpha_{\alpha\alpha}(0)\ \alpha_{\alpha\alpha}(t) >$). Note that as the molecule rotates, the components of the polarizability tensor in a fixed laboratory frame change as a function of the orientation of the molecule. In order to evaluate the orientation dependent correlation function $< \alpha_{\alpha\alpha}(0)\ \alpha_{\alpha\alpha}(t) >$, it is necessary to know the form of the polarizability tensor of the molecule and also assume some dynamical model for the rotational motions like rotational diffusion or free rotations. In section 2.4a, the explicit form of Eq. (2.3.11) will be given for VV and VH scattering from a system of cylindrically symmetric molecules undergoing rotational and translational diffusion.

Reproduced with permission of the copyright owner. Further reproduction prohibited without permission.

2.4 The origins of depolarized light scattering.[13]

As mentioned in chapter 1, MCT makes predictions for the behavior of the density fluctuations or other variables that couple strongly to the density fluctuations. In this section we explain briefly the origins of the low frequency depolarized spectrum as a result of orientational-fluctuations and collision(interaction)-induced scattering and relate this spectrum to the density fluctuations in the fluid.

2.4a:Orientational-fluctuation scattering:

When light interacts with a molecule, the electric field of the incident light induces a dipole moment. If the molecule is isotropic, the direction of the induced dipole will be the same as the incident electric field and the scattered light won't have any depolarized component. If the molecule is anisotropic, the magnitude and direction of the induced dipole depends on the orientation of the molecule. As a result, when the dipole radiates, in general its electric field will have, in addition to a polarized component, a component with a polarization different from the incident light, and both will fluctuate as the orientation fluctuates. This is the reason why the low-frequency scattered spectrum from a system of anisotropic molecules shows both polarized and depolarized spectra.

Anisotropic molecules are described by their polarizability tensor α. To illustrate the main physical ideas, consider a simple case of anisotropic molecules such as cylindrically symmetric molecules. In a molecule-fixed frame, the polarizability tensor in principal axes is:

Reproduced with permission of the copyright owner. Further reproduction prohibited without permission.

$$\alpha = \begin{bmatrix} \alpha_{//} & 0 & 0 \\ 0 & \alpha_{\perp} & 0 \\ 0 & 0 & \alpha_{\perp} \end{bmatrix} \qquad (2.4a.1)$$

where $\alpha_{//}$ and $\alpha_{\perp}$ are the polarizability components parallel and perpendicular to the symmetry axis respectively. The trace of the tensor ($\alpha_{//} + 2\alpha_{\perp}$) is invariant with respect to molecular orientations. For this reason, the molecular parameter α defined as:

$$\alpha \equiv (1/3)\,(\alpha_{//} + 2\,\alpha_{\perp}) \qquad (2.4a.2)$$

is called the isotropic part of the polarizability tensor (α is also the mean polarizability) . The parameter β defined as:

$$\beta \equiv \alpha_{//} - \alpha_{\perp} \qquad (2.4a.3)$$

is not invariant with respect to molecular orientations and measures the optical anisotropy of the molecule. For this reason, β is called the optical anisotropy or the anisotropic part of the polarizability tensor.

Consider that the position of the molecules are not correlated and that there is not coupling between translations and rotations; then, Eq. (2.3.11) for the correlation

Reproduced with permission of the copyright owner. Further reproduction prohibited without permission.

function holds. Consider also translational diffusion; then, Eq. (2.3.7) for F_s applies. Finally, consider rotational diffusion; then, the rotational ensemble averages in Eq.(2.3.11) can be calculated [13] for the VV and VH geometries.

$$\langle \alpha_{VV}(0)\alpha_{VV}(t)\rangle = \alpha^2 + \frac{4}{45}\beta^2 e^{-6\Theta t}$$

$$\langle \alpha_{VH}(0)\alpha_{VH}(t)\rangle = \frac{1}{15}\beta^2 e^{-6\Theta t}$$

So, the correlation function of Eq. (2.3.11), under all these conditions will be

$$C^{\alpha}_{VV}(q,t) = \langle N\rangle\left\{\alpha^2 + \frac{4}{45}\beta^2 e^{-6\Theta t}\right\}e^{-q^2 D t}$$

$$C^{\alpha}_{VH}(q,t) = \frac{1}{15}\langle N\rangle\beta^2 e^{-6\Theta t}e^{-q^2 D t}$$

From where the result for the spectral density by Fourier transform is (in the rest of the section we drop the superscript α for simplicity in the notation):

Reproduced with permission of the copyright owner. Further reproduction prohibited without permission.

$$I_{VV}(q,\omega)=\frac{<N>}{\pi}\left\{\alpha^2\frac{q^2D}{\omega^2+\left(q^2D\right)^2}+\frac{4}{45}\beta^2\frac{\left(6\Theta+q^2D\right)}{\omega^2+\left(6\Theta+q^2D\right)^2}\right\}$$

$$I_{VH}(q,\omega)=\frac{<N>}{\pi}\frac{\beta^2}{15}\left\{\frac{\left(6\Theta+q^2D\right)}{\omega^2+\left(6\Theta+q^2D\right)^2}\right\} \qquad (2.4a.4)$$

where D and Θ are the translational and rotational diffusion coefficients. If there is no anisotropy ($\beta = 0$), the spectrum only contains isotropic scattering. From Eq. (2.4a.4) we see that for isotropic scattering:

$$I_{VV}(q,\omega) = I_{ISO}(q,\omega) = \frac{<N>}{\pi}\alpha^2\frac{q^2D}{\omega^2+\left(q^2D\right)^2} \qquad (2.4a.5)$$

Thus, the VH spectrum for these cylindrically symmetric molecules originates only from anisotropic scattering, while the VV spectrum contains both isotropic and anisotropic scattering. From Eqs. (2.4a.4) and (2.4a.5), the relation among these components is:

$$I_{VV}(q,\omega) = I_{ISO}(q,\omega) + (4/3)\, I_{VH}(q,\omega) \qquad (2.4a.6)$$

We can integrate Eqs. (2.4a.4) and (2.4a.5) over ω to obtain:

Reproduced with permission of the copyright owner. Further reproduction prohibited without permission.

$$I_{ISO} = \langle N \rangle \alpha^2 \qquad (2.4a.7a)$$

$$I_{VH} = \langle N \rangle (1/15)\, \beta^2 \qquad (2.4a.7b)$$

$$I_{VV} = \langle N \rangle \alpha^2 + \langle N \rangle (4/45)\, \beta^2 \qquad (2.4a.7c)$$

Eq. (2.4a.6) also holds for the integrated intensities. The depolarization ratio $\rho_{iso} \equiv I_{VH}/I_{iso}$ is introduced as a measure of the relative contribution of the depolarized scattering with respect to isotropic scattering. From Eqs. (2.4a.7a-c) we get:

$$\rho_{iso} \equiv I_{VH} / I_{iso} = (1/15)(\beta/\alpha)^2 = (3/5)\,[\,(\alpha_{//} - \alpha_{\perp}) / (\alpha_{//} + 2\alpha_{\perp})\,]^2 \qquad (2.4a.8)$$

Eq. (2.4a.8) shows that the relative intensity of the depolarized scattering with respect to the isotropic scattering increases with the optical anisotropy β of the molecule. It is not possible experimentally to measure I_{ISO} directly; for this reason, the depolarization ratio defined in terms of the *VH* and *VV* scattered intensities by $\rho \equiv I_{VH} / I_{VV}$ is the one measured experimentally.

For dense systems like fluids, computer experiments [14] show that the cross correlation terms in Eq. (2.3.9) contribute very little in comparison with the self-terms. Then, to a good approximation, I_{VH} can be taken from Eq. (2.4a.7b). The isotropic part however, is reduced by interference effects, typically by a factor of 10-100 relative to Eq. (2.4a.7a).

Thus, we have seen that the anisotropy in the polarizability tensor of the molecules is responsible for the appearance of a depolarized scattered light component

Reproduced with permission of the copyright owner. Further reproduction prohibited without permission.

in the spectrum. This holds equally well for molecules with a more complicated anisotropic polarizability, but the theoretical treatment becomes more complex.

Finally, to relate the orientational-fluctuations depolarized scattering to density fluctuations in glass forming materials we need to incorporate the coupling between translations and rotations. Such a coupling, has been studied theoretically for molecular crystals possessing orientational disorder and is reviewed in [15]. Also, a molecular dynamics simulation of CKN [16], suggests that for that glass former, the orientational and translational dynamics are strongly coupled. However, for glass formers, the complexity introduced by the disordered structure, makes the theoretical treatment of the coupling still an unsolved problem.

2.4b.Collision-induced scattering:

Atoms are optically isotropic. Nevertheless, the spectrum of light scattered from monatomic gases shows a depolarized spectrum contrary to what could be expected from isotropic particles. The origin of this depolarized spectrum lies in the anisotropy induced among the atoms when they collide. This can be understood by realizing that when a pair of atoms are close together, their electron clouds get distorted and lose their isotropy. The polarizability of the combined system formed by two atoms interacting only with each other will be cylindrically symmetric along their internuclear vector. Due to the atomic motions, the orientation and value of the polarizability ellipsoid will fluctuate and we effectively return to the case of the orientational fluctuation scattering from cylindrically symmetric molecules. Thus the spectrum will show both polarized and depolarized components due to this collision-induced (or

Reproduced with permission of the copyright owner. Further reproduction prohibited without permission.

interaction-induced) scattering mechanism although the spectral shape is dominated by relative motion of the two atoms rather than orientational dynamics of the pair.

If we consider now the case of dense systems (like liquids) in which each atom interacts with several neighbors simultaneously, it is clear that if a given atom is surrounded by a spherically symmetric distribution of neighbors, no asymmetry will be induced in such an atom and no depolarized spectrum will be produced. Thus, in dense systems, I_{VH} can be regarded as being caused by density fluctuations that break the spherical symmetry of the cage surrounding any atom. So, in this case, we can relate the depolarized spectrum directly to density fluctuations in the medium.

The collision (interaction) scattering mechanism is frequently described in terms of the *dipole-induced dipole (DID)* model [17] as follows. The dipole moment p_i induced by the incident light in the i^{th} molecule, induces dipoles in its neighbors and all of them radiate at the same frequency. The fluctuations of the total dipole moment then produces the scattered spectrum. The spectrum was shown by Stephen [18] to be described by a convolution of pairs of density fluctuation modes, assuming the validity of a factorization approximation for four-point correlation functions into products of two-point functions:

$$I(q,\omega) \alpha \iint d^3 q_1 d\omega' S(q,\omega') S(|q - q_1|, \omega - \omega')$$

where S (q, ω) is the dynamical structure factor

Reproduced with permission of the copyright owner. Further reproduction prohibited without permission.

$$S(q,\omega) = \frac{1}{2\pi}\int_{-\infty}^{\infty} dt\, e^{-i\omega t}\left\langle \delta\rho^{*}(q,0)\delta\rho(q,t)\right\rangle \qquad (2.4b.1)$$

This result connects the depolarized light scattering spectrum to S(q, ω) which can then be compared with predictions of MCT [9].

The relative importance of *DID* versus orientational fluctuation scattering for the glass former Salol has been recently investigated by Cummins et al [19]. Their results indicate that for such a large and anisotropic molecule, the orientational fluctuation scattering is dominant with respect to *DID* scattering at all frequencies out to ~ $300\ cm^{-1}$. The authors also indicate that the same may be true for other glass formers composed of anisotropic molecules including glycerol.

Reproduced with permission of the copyright owner. Further reproduction prohibited without permission.

2.5 Quantum mechanical model for light scattering.

Quantum mechanically, first order inelastic light scattering is conceived as a process of creation (Stokes event) or annihilation (anti Stokes event) of a phonon [20]. The conservation laws of energy and momentum between the photons and the phonon are:

$$\omega_s = \omega_o - \omega \qquad \text{Stokes} \qquad (2.5.1a)$$

$$\mathbf{k}_s = \mathbf{k}_o - \mathbf{q}$$

and

$$\omega_s = \omega_o + \omega \qquad \text{anti Stokes} \qquad (2.5.1b)$$

$$\mathbf{k}_s = \mathbf{k}_o + \mathbf{q}$$

where ω_o and ω_s are the angular frequencies of the incident and scattered light while $\mathbf{k}_o$ and $\mathbf{k}_s$ are their wave vectors.

The quantum mechanical version of the fluctuation dissipation theorem, relates the intensity of the scattered light to the imaginary part of the susceptibility introduced in section 2.1 as follows

$$I(\mathbf{q}, \omega) \alpha [\, n(\omega) + 1 \,] \chi''(\mathbf{q}, \omega) \qquad (\text{Stokes}) \qquad (2.5.2a)$$

$$I(\mathbf{q}, \omega) \alpha\, n(\omega)\, \chi''(\mathbf{q}, \omega) \qquad (\text{anti Stokes}) \qquad (2.5.2b)$$

Reproduced with permission of the copyright owner. Further reproduction prohibited without permission.

where

$$n(\omega) = \frac{1}{e^{\frac{\hbar\omega}{KT}} - 1} \qquad (2.5.3)$$

For $\hbar\omega/KT \ll 1$; $n(\omega) \approx n(\omega) + 1 \approx KT/\hbar\omega$. Then, Eq. (2.5.2a,b) simplify to

$$I(q, w) \alpha \chi''(q, \omega)/\omega \qquad (2.5.4)$$

Reproduced with permission of the copyright owner. Further reproduction prohibited without permission.

2.6 The scope of light scattering experiments.

In Brillouin and Raman scattering, the light is inelastically scattered by acoustic and optic phonons respectively. The largest frequency shifts are observed in Raman scattering. Typically, these shifts are less than 3000 cm^{-1}, which corresponds to a vibrational frequency $f = 9x10^{13}$ Hz. Light with a wavelength of 600 nm has a frequency of the order of $5x10^{14}$ Hz, so, in the Brillouin scattering processes $\omega << \omega_o$. From Eq. (2.5.1) it follows that $\omega_o \approx \omega_s$ and by the relation $k = n\omega/c$ (where n is the index of refraction of the medium and c the speed of light) this implies that $k_o \approx k_s$. Under these circumstances, the relation among the wave vectors (for the anti-Stokes case) is as shown in Fig. 2.6.1 and the magnitude of the phonon wave vector is given by:

$$q = 2\, k_o \sin (\beta/2) \qquad (2.6.1)$$

For the incident light considered above, the maximum value of q is then $\approx 3x10^5$ cm^{-1}. This value is very small compared with the value $q = \pi/a \approx 10^8$ cm^{-1} at the boundary of the first Brillouin zone of a crystal of lattice constant $a \approx 0.3$ nm. This means that first order light scattering probes very small values of q close to the zone center and the scattering takes place in the so called long wavelength limit. The long wavelength acoustic modes involve in-phase motions of all the atoms in the unit cell and the atomic displacements are nearly constant over distances on the order of $\approx$ 100 unit

Reproduced with permission of the copyright owner. Further reproduction prohibited without permission.

cells. In this case the medium can be considered an elastic continuum and a macroscopic description can be used.

Reproduced with permission of the copyright owner. Further reproduction prohibited without permission.

2.7 Brillouin scattering

The existence of Brillouin scattering in a given direction can be understood in terms of Bragg scattering of light from sound waves. The Bragg planes here are imagined as the maxima of the sound waves which have a spacing equal to the sound wavelength Λ. The Bragg condition then establishes the relation between the wavelengths of the incident light and sound, and the scattering angle β, as:

$$\lambda = 2 \Lambda \sin (\beta/2) \qquad (2.7.1)$$

The frequency shift is accounted for by considering the Doppler shift of the light waves due to the propagating sound wave fronts. In the limit of small source speeds v relative to the speed of light c, the Doppler shifted frequency ω_s of the scattered light is:

$$\omega_s = \omega_o \pm 2vn (\omega_o/c) \sin (\beta/2) = \omega_o \pm 4\pi n (v/\lambda_o) \sin (\beta/2)$$

the Brillouin frequency shift is then:

$$\omega \equiv \omega_s - \omega_o = \pm 4\pi n (v/\lambda_o) \sin (\beta/2) \qquad (2.7.2)$$

For a given acoustic mode with velocity v, the scattered intensity is determined by the scattering tensor T through:

Reproduced with permission of the copyright owner. Further reproduction prohibited without permission.

$$I \alpha (1/v^2)(\hat{e}_s \cdot \mathbf{T} \cdot \hat{e}_o)^2, \qquad (2.7.3)$$

where $\hat{e}_o$ and $\hat{e}_s$ are the unit polarization vectors of the incident and scattered light respectively. To calculate **T** we first calculate the 6 component strain x_n as:

$$\begin{aligned} x_1 &= qu\,(\hat{q}_x \hat{u}_x); \\ x_2 &= qu\,(\hat{q}_y \hat{u}_y); \\ x_3 &= qu\,(\hat{q}_z \hat{u}_z); \\ x_4 &= qu\,(\hat{q}_y \hat{u}_z + \hat{q}_z \hat{u}_y); \\ x_5 &= qu\,(\hat{q}_x \hat{u}_z + \hat{q}_z \hat{u}_x); \\ x_6 &= qu\,(\hat{q}_x \hat{u}_y + \hat{q}_y \hat{u}_x), \end{aligned} \qquad (2.7.4)$$

where u is the magnitude of the local material displacement **u**, $\hat{q}_i = q_i / q$ and $\hat{u}_i = u_i/u$.

Multiplication of the six-component strain x_n by the 6 x 6 Pockels tensor p_{nm} produces the six component reciprocal dielectric constant ΔB_m.

$$B_m = \sum_{n=1}^{6} p_{nm} x_n \qquad (2.7.5)$$

The form of the Pockels tensor comes tabulated for different crystal symmetries in [21]. The 6 component ΔB are converted to a 3 x 3 form by:

Reproduced with permission of the copyright owner. Further reproduction prohibited without permission.

$$\begin{bmatrix} \Delta B_1 & \Delta B_6 & \Delta B_5 \\ \Delta B_6 & \Delta B_2 & \Delta B_4 \\ \Delta B_5 & \Delta B_4 & \Delta B_3 \end{bmatrix} = \begin{bmatrix} \Delta B_{11} & \Delta B_{12} & \Delta B_{13} \\ \Delta B_{21} & \Delta B_{22} & \Delta B_{23} \\ \Delta B_{31} & \Delta B_{32} & \Delta B_{33} \end{bmatrix} \qquad (2.7.6)$$

Then, the components of the scattering tensor **T** are found as :

$$T_{\alpha\beta} = (\Delta\beta_{\alpha\beta} / qu) \, . \, n^4 \qquad (2.7.7)$$

where n is the index of refraction of the scatterer.

Reproduced with permission of the copyright owner. Further reproduction prohibited without permission.

2.8 The technique of depolarized back-scattering spectroscopy:

In chapter 1 we mentioned that for the study of the dynamics of glass forming materials, we employed the technique of depolarized light scattering. This technique allows the measurement of signals from weak scattering processes like orientational-fluctuation and collision-induced scattering, both of which produce both polarized and depolarized spectra. The essence of the depolarized backscattering method consists in the supression of the strong Brillouin components in the spectrum from the longitudinal and transverse acoustic modes and the enhancement of the signal by increasing the effective scattering volume of the sample with respect to, for example, a 90° scattering experiment.

To understand the supression of the Brillouin modes, let us consider VH scattering from an isotropic material like a glass in the scattering geometry with **q** along the x direction as shown in Fig. 2.8.1, considering the three modes (one LA and two TA) separately. From [20] , the Brillouin scattering tensor for the LA mode is:

$$T = n^4 \begin{bmatrix} p_{11} & 0 & 0 \\ 0 & p_{12} & 0 \\ 0 & 0 & p_{12} \end{bmatrix}$$

With the help of Fig. 2.8.1 we can see that:

$$\hat{e}_o = \hat{y}(\mathrm{V}) \quad \text{and} \quad \hat{e}_s = -\hat{x}\cos(\beta/2) + \hat{z}\sin(\beta/2)$$

Reproduced with permission of the copyright owner. Further reproduction prohibited without permission.

Then, carrying out the matrix product from Eq. (2.7.3) we have:

$$I_L = 0 \ (VH)$$

so, the LA mode does not produce light scattering in the VH configuration, independently of the scattering angle β.

From [20], the Brillouin scattering tensor for the first TA mode, with **u** along the z direction is:

$$T = n^4 \begin{bmatrix} 0 & 0 & \frac{p_{11} - p_{12}}{2} \\ 0 & 0 & 0 \\ \frac{p_{11} - p_{12}}{2} & 0 & 0 \end{bmatrix}$$

A similar calculation for this TA mode as the one done for the LA mode above shows that this mode does not produce light scattering either.

From [20], the Brillouin scattering tensor for the second TA mode, with **u** along the y direction is:

Reproduced with permission of the copyright owner. Further reproduction prohibited without permission.

$$T = n^4 \begin{bmatrix} 0 & \frac{p_{11}-p_{12}}{2} & 0 \\ \frac{p_{11}-p_{12}}{2} & 0 & 0 \\ 0 & 0 & 0 \end{bmatrix}$$

Then if the same calculation as above is performed for this TA mode, the result is:

$$I\alpha\left(\frac{p_{11}-p_{12}}{2}\cos(\beta/2)\right)^2$$

so, this TA mode does produce depolarized light scattering, but the intensity is zero in the back-scattering geometry ($\beta = 180°$).

We thus see that in a back-scattering, VH experiment from a glass, the Brillouin modes are ideally eliminated; the LA mode and one of the TA modes because they are forbidden in the VH configuration and the other TA mode because its intensity vanishes for $\beta = 180°$. We can not eliminate Brillouin scattering in the VV configuration (by a similar calculation, it can be shown that the intensity for the LA mode is independent of the scattering angle). In the case of a normal liquid sample, we have the simplifying fact that there are no TA modes because a liquid does not support shear waves (supercooled liquids, however, do support shear waves).

Reproduced with permission of the copyright owner. Further reproduction prohibited without permission.

To finish this section, let us mention that our experiments were done in near back scattering ($\beta = 173°$). According to our discussion above, we should not have complete extinction of the TA mode in the glassy state. This does not affect much our results because on the one hand at this large scattering angle, the scattering is weak, and on the other, most of our measurements were done in the liquid state where there are no TA modes. LA modes, which should be completely eliminated, do nevertheless appear in the spectra at low temperatures due to leakage through imperfect polarizers.

Reproduced with permission of the copyright owner. Further reproduction prohibited without permission.

2.9 The tandem, multipassed Fabry-Perot interferometer

In this section we provide a basic description of the conventional and tandem multipassed Fabry-Perot interferometers. In our measurements we use a Sandercook, tandem, multipassed Fabry-Perot interferometer.

Consider first a conventional Fabry-Perot interferometer described in many general optics texts like [22]. It consists of two parallel mirrors separated by a distance d as shown in Fig. 2.9.1. The inner surfaces of the mirrors are coated with a thin reflective metal (or multilayer dielectric) film. The surface is characterized by its reflectivity R, transmitivity T and absorptivity A. Conservation of energy requires that $R + T + A = 1$. The interference pattern is a result of multiple beam interference from parallel light beams forming the same angle θ with respect to the axis of the interferometer as shown in Fig. 2.9.1. Constructive interference occurs if the condition:

$$m \lambda = 2 n d \cos \theta \qquad (2.9.1)$$

is satisfied. The integer m is the order of interference, n is the refractive index of the medium between the mirrors (usually air with $n \approx 1$) and λ is the wavelength of the light. A typical transmission pattern (relative transmission vs d for $\theta = 0$) could look like one of the curves shown in Fig. 2.9.2. This central spot scanning approach is almost always used in modern spectroscopic applications of the Fabry-Perot) The pattern consists of a series of equally spaced interference maxima. Several quantities

Reproduced with permission of the copyright owner. Further reproduction prohibited without permission.

are used to characterize the interferometer like the free spectral range FSR, finesse F, transmission function T_r, and the contrast C.

The free spectral range FSR is defined as the equivalent change in frequency (or wavelength) corresponding to the difference between adjacent maxima for fixed frequency. The importance of the FSR is that it tells us the maximum allowed bandwidth of the light signal to avoid overlapping of different interference orders in the same spectral region. It can be calculated as:

$$FSR\ (Hz) = c / (2\ n\ d) \qquad (2.9.2)$$

where c is the speed of light.

The finesse F is defined as the ratio of the FSR to the full width at half maximum δf of a given transmission peak:

$$F \equiv FSR / \delta f \qquad (2.9.3)$$

Thus, the finesse is a measure of the instrumental broadening and therefore determines the resolution. The instrumental broadening is determined by the reflectivity of the mirrors, the surface roughness and the collimation of the incident light.

The transmission function T_r (or instrumental function) is defined as the ratio between the transmitted and incident intensities. It can be calculated as:

Reproduced with permission of the copyright owner. Further reproduction prohibited without permission.

$$T_r = \left(\frac{T}{1-R}\right)^2 \frac{1}{1+\frac{4}{\pi^2}F^2\sin^2\frac{\delta}{2}} \qquad (2.9.4)$$

where $\delta = (4\pi/\lambda)\, n\, d \cos\theta$. Fig. 2.9.2 shows this function for several values of the finesse.

The contrast C is defined as the ratio of the maximum to minimum transmitted intensities. This quantity characterizes the ability of the instrument to detect weak spectral components when an intense component is present at a nearby frequency. It is shown to be:

$$C = 1 + (2F/\pi)^2 \qquad (2.9.5)$$

The main disadvantages of a conventional Fabry-Perot for Brillouin spectroscopy are the low contrast and the overlapping of orders. These difficulties can be overcome by using a multipassed tandem Fabry-Perot interferometer as explained below. In a tandem interferometer the light passes through two single Fabry-Perot interferometers operated at different spacing. Multipassing means that the light passes repeatedly through the interferometer.

The contrast can be increased by multipassing. Ideally, for a Fabry-Perot passed N times, the contrast will be:

$$C_N = C^N = [\,1 + (2F/\pi)^2\,]^N \qquad (2.9.6)$$

Reproduced with permission of the copyright owner. Further reproduction prohibited without permission.

The overlapping of orders can be eliminated by putting in tandem two cavities of different spacings d_1 and d_2 . Light will only be transmitted through the pair when the conditions for maxima are satisfied simultaneously in the two cavities.

$$m_1 \lambda = 2 n d_1 \cos\theta \; ; \qquad m_2 \lambda = 2 n d_2 \cos\theta \qquad (2.9.7)$$

The transmission function of the combined system is the product of the transmission functions of each cavity. The transmission functions for each cavity and for the tandem combination is shown in Fig. 2.9.3. From the figure we can see that most orders are suppressed in the combined pattern. This supression continues for several orders until the conditions in Eq. (2.9.7) are again satisfied simultaneously. As a result, the effective FSR of the tandem instrument increases by a factor equal to the number of consecutive orders suppressed and the frequencies that could produce overlapping will be more separated from the central frequency and can be removed easily by a frequency filter. In practice, the tandem interferometer is scanned electronically and the alignment is continuously adjusted electronically. The transmitted signal is focused onto a photomultiplier tube whose output, measured as a sequence of digital photocounts, is stored in a computer for subsequent data analysis.

Reproduced with permission of the copyright owner. Further reproduction prohibited without permission.

2.10 Raman spectroscopy

Depolarized Raman spectra were collected with a Spex 1401 double grating monochromator equipped with holographic gratings and a computer controlled stepping motor. The optical layout is shown in Fig. 2.10.1. The excitation light is the 488 nm line of a Coherent 52 Argon laser. The excitation beam is focused on the sample by lens L_1. The incident light is vertically polarized. Scattered light is collected at a near-back scattering angle of 173^0 by the lens L_2 and is focused on the spatial filter SF which selects the scattering volume of the sample. The polarizer P selects the polarization component of the scattered light. The lens L_3 collimates the beam. A polarization scrambler S is used to produce unpolarized light in order to average the polarization efficiency of the monochromator. The lens L_4 matches the entrance solid angle and focuses the beam on the entrance slit. The entrance, middle, and exit slits of the spectrometer are usually set to 100, 200 and 100 μm respectively. With these widths, the spectral resolution is approximately 1 cm^{-1}. The PMT signal is integrated, discriminated, amplified and sent to the data acquisition card on the computer where it is digitally stored for future data processing.

Reproduced with permission of the copyright owner. Further reproduction prohibited without permission.

2.11 FTIR spectroscopy

The Fourier Transform Infrared (FTIR) spectrometer used is a BRUKER IFS 66. The instrument uses as IR source a globar which produces radiation in the near, middle or far IR spectrum. The radiation passes first through a Michelson interferometer, then through the sample and finally reaches the detector. The interference pattern at the detector is time dependent due to the scanning movement of the movable mirror of the interferometer. The time dependent pattern is recorded digitally, then automatically Fourier transformed to produce the frequency domain spectrum of the transmitted radiation.

For measurements concerning molecules in solution as in our case, the spectral contribution from the solvent must be subtracted. To achieve this, the solvent and sample are loaded into different cells. Both cells are mounted on a common cell holder that is attached to a computer controlled translation stage. The stage exposes alternatively the solvent or sample solution to the IR radiation for short periods of time. Such a cycle is repeated several times until the desired signal to noise ratio is obtained. This procedure is intended to decrease the effects of changing experimental conditions.

Reproduced with permission of the copyright owner. Further reproduction prohibited without permission.

3. DYNAMICS OF GLASS FORMING MATERIALS

3.1 Introduction

If a material does not crystallize upon cooling below the melting temperature, the liquid will enter an undercooled state. If cooling is sufficiently rapid so that crystallization does not occur for even lower temperatures, the glassy state will be reached in which the material is an amorphous solid. The disordered nature of the molecular structure of the liquid will persist in the glass. Quantities like the viscosity will change continuously as a function of the temperature. Conventionally, the glass transition temperature T_g (also called calorimetric glass transition temperature) is defined as the temperature at which the viscosity reaches 10^{13} *Poise*. Glycerol is an example of a very good glass former. It can be cooled below its melting temperature at very slow cooling rates without undergoing crystallization.

The viscosity of glass forming liquids changes dramatically from about 10^{-2} *Poise* for a liquid well above the melting temperature T_m to 10^{13} *Poise* at T_g. Following the terminology of C. A. Angel, materials for which the viscosity changes with T much faster than an Arrhenius law $\eta=Ae^{(B/T)}$ are called fragile glass formers; if they show Arrhenius behavior they are called strong glass formers. Materials exhibiting behavior between these two extremes are called intermediate glass formers. The reduced Arrhenius plot shown in Fig. 3.1.1, usually called an Angel plot [23], serves to classify the fragility of glass formers by the location of their viscosity-temperature curves in such a plot. The presence and strength of networks determines if a material is

Reproduced with permission of the copyright owner. Further reproduction prohibited without permission.

a strong, intermediate or fragile glass former. In the fused salt glass former CKN ($CaKNO_3$), the molecules do not form any network while in silica glass, they form a very strong covalent bond network. CKN and silica are fragile and strong glass formers respectively. Glycerol molecules form a weak network of hydrogen bonds and glycerol is an intermediate material.

Structural relaxation in glass forming liquids has been studied using a variety of techniques like dielectric susceptibility [24], neutron [7] and light scattering [9], just to mention some of them. The primary *α– relaxation* appears as a very strongly temperature dependent spectral feature as can be seen in Fig. 3.1.2 for the dielectric susceptibility $\varepsilon''(\omega)$ of glycerol from Ref. [25]. The *α–peak* in the χ'' spectrum is stretched (width larger than the Debye or single exponential relaxation case) and asymmetric. The neutron or light-scattering spectrum recorded over a very wide frequency range (Fig. 3.1.3), typically shows two broad bands and a minimum in between. The lower frequency band is the already mentioned *α–peak* and the higher frequency one is called the *boson-peak*. The region around the minimum in $\chi''(\omega)$ in the mode coupling nomenclature [26, 27] is called the *β–relaxation* region. The spectrum in this *β* region has properties different from the *α-region*; it is less temperature sensitive and satisfies different scaling laws. The discovery of the properties of the spectrum in this region is a recent event and has received a lot of attention in the last 10 years.

For glycerol, the *β–relaxation* region lies in the GHz frequency window. Currently, the high frequency limit for dielectric loss measurements extends up to

Reproduced with permission of the copyright owner. Further reproduction prohibited without permission.

about 40 GHz, so, this spectroscopy is not very suitable in this relaxation regime. Neutron scattering spectroscopy can extend from about 10 GHz to the THz region and constitutes a very good probe. The combination of interferometric and diffraction grating light scattering spectroscopy allows coverage from the MHz to the THz region, thus, having also a wide dynamical range. In addition, light scattering experiments easily provide a much better signal to noise ratio than neutron scattering and can be conducted in a simple laboratory setting, in contrast to the need of a nuclear reactor for neutron scattering experiments.

Reproduced with permission of the copyright owner. Further reproduction prohibited without permission.

3.2 Mode coupling theory for the liquid to glass transition.

A liquid, considered as a classical system is governed by the equations of motion of classical mechanics. Consider an arbitrary mechanical property A of the system, which in general, depends on the positions and momenta of all particles. If this is the only dynamical property needed to describe the system, then, the time evolution of the correlation function $C_A(t)$ (also called a mode) of A can be formally obtained [28] from the generalized Langevin (or Zwanzig-Mori) equation

$$\ddot{C}_A(t)+\Omega_A^2 C_A(t)+\int_0^t dt' M_A(t-t')\dot{C}_A(t')=0 \qquad (3.2.1)$$

where M_A is called a memory function and Ω_A is a microscopic frequency. This equation resembles the familiar equation for a damped harmonic oscillator, but now, the damping term is replaced by a frequency-dependent damping function, expressed as a memory integral; the damping at time t depends on the previous states, with weight specified by the memory function $M_A(t- t')$.

Equation (3.2.1) is formally exact. It shows that the problem of finding $C_A(t)$ is transferred to the determination of the memory function. MCT is one of several approaches used to determine the memory function. MCT calculations were originally developed by Kawasaki who applied them in 1970 to the study of critical phenomena [1].

Reproduced with permission of the copyright owner. Further reproduction prohibited without permission.

In 1984, the first papers appeared [2] and [3] with the application of the MCT formalism to the problem of the liquid to glass transition in simple liquids of spherical molecules. The important regime here is the long time limit of the dynamics. The relevant variables of the problem are the density fluctuations with wavevector q. When the mode coupling approximation is introduced and made specific for the case of dense liquids, Eq. (3.2.1) becomes an equation of motion for the normalized autocorrelation function for density fluctuations with wavevector of modulus q:

$$\phi_q(t) = \frac{\left\langle \rho_q(0)\, \rho_q(t) \right\rangle}{\left\langle \left| \rho_q(t) \right|^2 \right\rangle}$$

$$\ddot{\phi}_q(t) + \Omega_q^2 \phi_q(t) + \int_0^t dt'\, M_q(t-t')\, \dot{\phi}_q(t') = 0 \qquad (3.2.2a)$$

The memory function $M_q(t)$ is split into an instantaneous normal damping term and a second term $m_q(t)$ representing slowly relaxing fluctuations.

$$M_q(t) = \nu_q\, \delta(t) + \Omega_q^2\, m_q(t) \quad , \ \nu_q > 0 \qquad (3.2.2b)$$

$$m_q(t) = \sum_{n=1}^{m_0} \left(\frac{1}{n!} \right) \sum_{q_1 \cdots q_n} V^{(n)}(q, q_1, \ldots, q_n)\, \phi_{q_1} \cdots \phi_{q_n}$$

Reproduced with permission of the copyright owner. Further reproduction prohibited without permission.

$$m_q(t) = \sum_{q_1} V^{(1)}(q,q_1)\phi_{q_1} + \frac{1}{2}\sum_{q_1,q_2} V^{(2)}(q,q_1,q_2)\phi_{q_1}\phi_{q_2} + \ldots \qquad (3.2.2c)$$

The coefficients $V^{(m)}$ are called coupling constants or vertices. They are expressed in terms of the static structure factors S(q), which, in turn, can be calculated from the intermolecular potentials. The memory function in Eq. (3.2.2b) is separated in a fast term ($\nu_q \delta(t)$) to represent the fast dynamics, and a slow term $m_q(t)$, responsible for the non linearities and memory, which determines the slow dynamics of the system. Eq.(3.2.2c) shows how the mode q is coupled to the other modes $q_1,\ldots q_m$.

Eqs. (3.2.2a-c) are a closed set of equations for the $\phi_q(t)$ which are coupled via the relaxing part $m_q(t)$ of the memory function $M_q(t)$. The equations can be solved numerically if the potentials are given. The dominant contributions to $m_q(t)$ come from the bilinear terms in Eq. (3.2.2c), which represent the coupling of the mode q to the pair of modes q_1 and q_2 in the bilinear product. Using just these bilinear terms, the equations have been solved numerically for hard sphere [3] and Lennard-Jones [29] systems.

It was found [3] that the main contribution of S(q) to the memory function comes from the main peak in S(q). Then, to simplify the numerical solution of the system of equations, S(q) was approximated by

$$S(q) \approx 1 + \delta(q_0) \qquad (3.2.3)$$

Reproduced with permission of the copyright owner. Further reproduction prohibited without permission.

where q_0 is the magnitude of the wave vector corresponding to the maximum of S(q). Thus, only modes with the same magnitude of the wave vector are considered. In this case, all relevant modes have the same magnitude of q and are equivalent by symmetry; therefore such labeling can be dropped. The system of equations then reduces to a single equation of type (3.2.2a) without the label q. The models obtained by this approximation are the simplest possible to treat and are called schematic models. The memory function for these schematic models can contain linear, bilinear, or higher order terms, depending on the kind of terms selected from Eq. (3.2.2c). Some of these models are:

F_2 model: Specified by $m(t) = v^{(2)} \phi^2(t)$ (3.2.4)

F_{12} model: Specified by $m(t) = v^{(1)}\phi(t) + v^{(2)}\phi^2(t)$ (3.2.5)

The simple F_{12} schematic model exhibits stretched α-relaxation while the F_2 model does not. Numerical solutions for $\phi(t)$ and $\chi''(\omega)$ obtained with the F_{12} model are shown in Fig. 3.2.1a,c which is reproduced from [30]. Different curves correspond to different values of the coupling constants which become larger with increasing density (or equivalently, with decreasing T). The model predicts a liquid to glass transition in the sense that with decreasing T, a critical temperature T_c is reached, such that, for $T \leq T_c$, the correlation function does not decay to zero for very large times. Curves F', D' and B' in Fig. 3.2.1a represent such cases. Thus, crossing T_c from above, an

Reproduced with permission of the copyright owner. Further reproduction prohibited without permission.

ergodic to non-ergodic transition occurs. The MCT treatment explained so far is called the idealized MCT.

The use of idealized MCT predictions (to be discussed below) for real systems shows that $T_c > T_g$. However, the viscosity and dielectric susceptibility of supercooled liquids are known to change smoothly and continuously with decreasing T, demonstrating that structural arrest can not take place above T_g. This contradiction with the idealized MCT was resolved after Das and Mazenko [31] proposed to include terms involving currents in the memory function. Goetze and Sjoegren [30,32] extended the theory in this way, developing the so called extended version of the MCT. The extended version differs from the simplified case by the form of the memory function M_q (t). In Laplace transformed variables $M_q(z)$ is

$$M_q(z) = \frac{\Omega_q^2 \left[i\upsilon_q + m_q(z) \right]}{1 - \delta_q(z)\Omega_q^2 \left[i\upsilon_q + m_q(z) \right]} \tag{3.2.6}$$

The current term δ_q (t), expressed in terms of the dominant bilinear couplings only, is given by

$$\delta_q(t) = \sum_{q_1 q_2} V'(q, q_1, q_2)\, \dot{\phi}_{q_1}(t)\, \dot{\phi}_{q_2}(t) \tag{3.2.7}$$

Reproduced with permission of the copyright owner. Further reproduction prohibited without permission.

The numerical solution of the extended schematic model F_{12} was also carried out [30]. We reproduced their results in Fig. 3.2.1b,d. As we see, now the correlation function eventually decays to zero also for $T < T_c$ restoring the α-relaxation peak. The simplified MCT is an approximation to the extended version. However, its predictions are simpler than those of the extended theory, and for $T > T_c$ some results are identical in both. For these reasons, we limit our subsequent analysis to the idealized version.

Predictions of the idealized MCT

Here we mention a few predictions of MCT. We are interested in the so called β–relaxation region, the region between the α–relaxation and the microscopic excitations. This region in Fig. 3.2.1c,d corresponds to the region surrounding the minimum in $\chi''(\omega)$ or the inflection point in $\phi(t)$.

In the glass transition scenario, the external control parameters (like temperature), determine the coupling constants of the system, so, by changing the control parameters we can reach the glass transition point in parameter space. Several analytical results are obtained, which are valid in the vicinity of the transition point; the distance from which is characterized by the separation parameter σ

$$\sigma \propto (T_c - T) / T_c \qquad (3.2.8)$$

Reproduced with permission of the copyright owner. Further reproduction prohibited without permission.

The results are obtained as asymptotic expansions around the glass-transition-singularity (GTS). In leading order, we can mention the following results:

The normalized autocorrelation function obeys the factorization of the time and wavevector dependence.

$$\phi_q(t) = f_q^c + h_q\, G(t) \tag{3.2.9}$$

Here f_q^c is the infinite time limit of the correlation function at the critical temperature T_c, the factor h_q is called critical amplitude. The relaxing part G(t) is also called the β–correlator and satisfies the scaling law

$$G(t) = |\sigma|^{1/2} g_{\pm}(t/t_\sigma) \tag{3.2.10}$$

The + or - signs correspond to T below or above T_c respectively. The scaling time t_σ is proportional to $|\sigma|^{-2a}$ and a, which is called the critical exponent, is determined by the system dependent exponent parameter λ from Eq. (3.2.13). The functions g_+ and g_- are the master functions for the glass and liquid dynamics, which depend on the rescaled time t/t_σ. The susceptibility spectrum $\chi''(\omega)$ satisfies the scaling equation

$$\chi''_q(\omega) = h_q |\sigma|^{1/2} \hat{\chi}''_{\pm}(\omega/\omega_\sigma) \tag{3.2.11}$$

Reproduced with permission of the copyright owner. Further reproduction prohibited without permission.

where $\hat{\chi}^{\cdot}_{\pm}$ are the susceptibility master functions and ω_σ is the scaling frequency $\omega_\sigma = 1/t_\sigma$.

The master function for $T > T_c$ can be approximated by the interpolation formula.

$$\chi''(\omega/\omega_{min}) = \chi''_{min}\left[b\left(\frac{\omega}{\omega_{min}}\right)^{a} + a\left(\frac{\omega_{min}}{\omega}\right)^{b}\right]^{\frac{1}{a+b}} \qquad (3.2.12)$$

where:

ω_{min} is the angular frequency at the minimum and is approximately equal to ω_σ.

χ''_{min} is the susceptibility minimum

a and b are the critical exponents and are determined by the exponent parameter λ via the gamma function relation

$$\lambda = \frac{\Gamma^2(1-a)}{\Gamma(1-2a)} = \frac{\Gamma^2(1+b)}{\Gamma(1+2b)} \qquad (3.2.13)$$

From this equation, the critical exponents are restricted to the ranges $0 \leq a \leq 0.395$, $0 \leq b \leq 1$.

Eq. (3.2.12) interpolates between the so called critical spectrum $\chi''(\omega) \alpha \omega^{a}$ and the Von Schweidler spectrum $\chi''(\omega) \alpha \omega^{-b}$ which is the high frequency tail of the α–relaxation.

Reproduced with permission of the copyright owner. Further reproduction prohibited without permission.

We must note that this interpolation formula is just the first order approximation to the master function. Also, the master function is itself a leading order asymptotic result for an expansion around the critical point.

From the scaling law for the susceptibility (Eq. (3.2.11)) it follows that

$$\chi''_{min} \alpha (T - T_c)^{1/2} \qquad (3.2.14)$$

and

$$\omega_{min} \alpha (T - T_c)^{1/2a} \qquad (3.2.15)$$

Equations (3.2.14,15) predict a linear behavior in a plot of χ''^2_{min} or ω^{2a}_{min} vs T respectively. From such a plot, we can get a first estimate of T_c as the intercept on the T axis.

Reproduced with permission of the copyright owner. Further reproduction prohibited without permission.

3.3 Previous tests of MCT.

The first attempts to verify the MCT predictions were mainly centered in the identification of the critical temperature T_c and the critical decay spectrum ($\phi(t) \alpha t^{-a}$ or $\chi''(\omega) \alpha \omega^{a}$). Most of the experiments were inelastic neutron scattering, e.g. ([4], [5], [6], [7], [8], [33]). The analysis of the results confirmed the existence of a critical temperature T_c, different from the calorimetric glass transition temperature T_g, such that above and below it, the dynamical behavior of the system was qualitatively different. The experiments also revealed the critical spectrum and showed that the scattering intensity in this region was larger than the one expected from the contributions of the low frequency tail of the α-relaxation, plus a white noise between this long frequency tail and the microscopic band. These experiments are discussed in the review article by Goetze and Sjoegren [26].

The recent development of the light scattering technique called depolarized near-back scattering, explained in section 2.4, has also allowed measurements in the β-relaxation regime. One of the advantages of light scattering over neutron scattering measurements is a much better signal to noise ratio, specially for low temperatures. This technique has been used in our laboratory in the spectral range $0.3\text{GHz} \leq \omega/2\pi \leq 5{,}000\text{GHz}$ for the fragile glass formers Calcium Potassium Nitrate (CKN) [9], salol [10] Propylene Carbonate (PC) [11] and orthoterphenyl (OTP) [12]. The spectra show the scaling behavior predicted from Eq. (3.2.10). The interpolation formula (3.2.12) was found to adequately describe the data with values of the parameter a and b consistent with the λ constraint specified by Eq. (3.2.13). Also,

Reproduced with permission of the copyright owner. Further reproduction prohibited without permission.

$(\chi''_{min})^{1/2}$ and $(\omega_{min})^{2a}$ vs T behaved linearly according to Eq. (3.2.14,15) over a surprisingly large range of T.

In reference [34], the data from references [9] and [10] was reanalyzed with the extended MCT. The results showed an improvement of the agreement between theory and experiments and removed some contradictions observed for low frequencies at temperatures near and below T_c. Similar improvement for PC was found in [11].

Therefore, it is now clear that MCT is able to explain several non trivial phenomena in fragile glass formers. One could also ask, how well the theory can predict the dynamical behavior of non-fragile glass formers like glycerol, for which the theory was not intended. Our glycerol experiments described in the next sections were intended to find an answer to that question.

Reproduced with permission of the copyright owner. Further reproduction prohibited without permission.

3.4.1 Experiments

We selected glycerol as the glass forming material with which to test the applicability of MCT to intermediate glass forming materials. Glycerol [$C_3H_3(OH)_3$], with a melting temperature T_m = 291 K is a liquid at room temperature. It can be undercooled to its conventional glass transition temperature T_g = 185K at very slow cooling rates without undergoing crystallization. Its molecules form a weak network of hydrogen bonds, making it intermediate between fragile and strong glass formers. Preliminary results of both light-scattering and neutron scattering experiments were reported in [35].

For our light scattering experiments glycerol was purchased from Aldrich (99.5+% pure, lot no. 05961AZ) . The material was used directly as provided without further purification. Using syringes, the liquid was transferred from the container to the sample cells under a controlled atmosphere of nitrogen to avoid absorption of water vapor. We used cylindrical glass cells of 12 mm diameter and 16 mm height; they were filled up to about 13 mm, then flame sealed at the top under vacuum.

The cell was put inside a copper holder. Silver paint was applied between the bottom of the cell and the holder to facilitate conductive heat transfer. The holder was attached to the cold finger of an Oxford ND1754 cryostat which allowed heating or cooling in the range 173 to 413 K. The temperature in the cryostat was automatically controlled to ±0.1K with an Oxford ITC4 temperature controller.

In the near back-scattering experiments we used a scattering angle $\beta = 173^0$. At this angle, the scattering from the TA mode of the supercooled liquid or the glass is

Reproduced with permission of the copyright owner. Further reproduction prohibited without permission.

almost completely suppressed as was explained in section 2.8. In that section we also mentioned that the VH spectra show a narrow line due to leakage of the LA Brillouin line through the imperfect polarizer. We removed this "leaked" line by subtracting the appropriately scaled VV-polarized scattering component.

In the Raman measurements we only recorded the Stokes side of the spectrum. In Brillouin scattering, both the Stokes and anti-Stokes spectra were recorded. For data processing, we used the averaged Brillouin scattering intensity I_B as follows

$$I_B(\omega) = [\, I_S(\omega) + I_{AS}(-\omega) \,] / 2$$

where I_S and I_{AS} are the Stokes and anti-Stokes scattering intensities.

The tandem interferometer was used at four different mirror spacings (which determine the FSR by Eq. (2.9.2)) ranging from d = 25 mm to d = 0.45 mm. The mirror separations are selected in such a way, that the spectra corresponding to contiguous spacings overlap over a sufficiently large frequency range. This allows the splicing of the contiguous spectra where the slope of the spectrum is the same for both spectra. In this way, several Brillouin spectra, corresponding to different mirror spacings, and one Raman spectrum; can be spliced to produce a composite spectrum over a frequency range covering four decades. The described process of averaging and splicing is illustrated in Fig. 3.4.1. In this splicing, the spectra obtained with d=2mm were used as the reference, this set having been obtained with careful monitoring of laser intensity.

Reproduced with permission of the copyright owner. Further reproduction prohibited without permission.

A composite spectrum as described above, was obtained from the spectra measured at each temperature (173, 193, 203. 213, 223, 233, 243, 253, 263, 273, 293, 313, 333, 363 and 413 K). In order to facilitate the comparison of the spectra to MCT predictions, the intensity spectra were converted to dynamic susceptibility spectra $\chi''(\omega)$ as indicated in Eq. (2.5.2). The susceptibility spectra for all temperatures are represented in Fig 3.1.3. A log-log plot is needed in order to show all the data. The vertical axis relative calibration was obtained by calculating the normalized number of photocounts of the intensity files in a small frequency interval from 25 to 35 GHz.

Reproduced with permission of the copyright owner. Further reproduction prohibited without permission.

3.4.2 Results

The susceptibility spectra of Fig. 3.1.3 show an essentially temperature independent broad band centered around 1.1 THz. This region corresponds to vibrational excitations. The band is commonly called boson peak (or microscopic peak). Its strength increase from fragile to strong glass formers. Several possible explanations of its origin have been proposed; however, none of them has yet been shown to be correct. Here we are only interested in the relaxation spectrum. Therefore, no further comments about the boson peak will be given. A brief description of the most important proposed explanations and citations to original papers can be found in [36].

The spectra also show a low frequency band, easily visible for higher temperatures ($T \geq 313$ K). This band is the α-relaxation peak which moves dramatically to higher frequencies with increasing temperature. This highly T sensitive relaxation has been extensively studied by dielectric and other relaxation techniques. MCT also makes some predictions about it. Our frequency window however, is only large enough, to show at most, just part of the α-relaxation peak for the higher T spectra. Here, we are not concerned about α-relaxation either, so, no further comments will be made about it. A description of some of the characteristics of α-relaxation and its relation to MCT can be found in [26] and references therein.

In this work we are interested in the β-relaxation region, the region around the minimum of the susceptibility spectra, between the α-relaxation and boson peaks. Below, we compare our data with some MCT predictions.

Reproduced with permission of the copyright owner. Further reproduction prohibited without permission.

a) Scaling properties of the spectra.

We begin our comparison between MCT predictions and the data, by making a scaling plot of $\chi''(\omega)$ for those spectra showing a minimum. To Achieve this, we normalize the frequency and susceptibility axes as ω/ω_{min} and $\chi''(\omega)/\chi''_{min}$ respectively; where ω_{min} and χ''_{min} are the values of the frequency and susceptibility at the susceptibility minimum. The scales ω_{min} and χ''_{min} were obtained, by fitting spectra individually with a non-linear-least-squares fitting routine to the interpolation formula Eq. (3.2.12), keeping a and b as free fitting parameters. The resulting χ''_{min} and f_{min} values are shown in table 1. With this normalization, the susceptibility spectra coincide at their minima.

The resulting scaling plot is shown in Fig. 3.4.2 for temperatures ranging from 243 to 413 K (lower points). This figure also contains a scaling plot for neutron scattering data (upper points) obtained by Wuttke [35] (open circles , temperatures from 270 to 413 K), which we have included for comparison. For clarity, the neutron data have been shifted upward by a factor of 3.

The light scattering data show that the group of spectra corresponding to temperatures from 273 to 413 K superimpose on each other over some frequency range. This overlap of the normalized spectra means that they obey some scaling law. We can also see that the frequency range over which the overlapping is observed increases as the temperature decreases from 413 to 273 K. This expansion of the scaling region as $T \rightarrow T_c$ is one of the central predictions of MCT.

Reproduced with permission of the copyright owner. Further reproduction prohibited without permission.

On the other hand, the spectra for the group corresponding to the temperatures 263, 253 and 243 K, separate on the high frequency side from the other spectra. Also, these three spectra do not overlap with each other over a frequency range as large as the one observed for the other group. We should also notice the perturbing fact that these "problematic" spectra correspond to temperatures which we expect to be closer to the MCT critical temperature T_c; however, MCT predicts that the scaling function is more accurately obeyed closer to T_c and also, that the scaling range should increase as T_c is approached.

We could still say that all spectra show the same scaling behavior over a small frequency range around the susceptibility minimum. If the frequency range in increased, however, the overall scaling is broken.

We can summarize these results by saying that for the intermediate glass-former glycerol, the spectra show scaling behavior in the β-relaxation region only over a very small range of temperatures and frequencies, in contrast to the much larger ranges observed from experiments on fragile materials like salol [10] and others.

b) Quantitative tests of MCT scaling.

Next, we want to see, if the limited range scaling described in *a)* obeys the MCT interpolation formula Eq. (3.2.12). To fit the data, we make a global fit. Global means that the data for all temperatures considered, is described by a single set of exponents *a* and *b*. The fitting range for each spectrum is obtained from its limited

Reproduced with permission of the copyright owner. Further reproduction prohibited without permission.

scaling range, as determined from Fig. 3.4.2. We made two kinds of fits as described below.

First, we let a and b to be free parameters. From the fitting we obtained $a=0.54$ and $b = 0.43$. These fits are shown in Fig. 3.4.3 with solid lines. We see that the fits reproduce the data in the selected range reasonably well. However, the results clearly violate the MCT constraint on the value of the parameter a, because the β–relaxation scaling law requires via the constraint Eq. (3.2.13) that a must be less than 0.395.

Our second fit was a constrained one, in which a and b were forced to obey the gamma function relation Eq. (3.2.13). This time we obtained $a=0.32$ and $b=0.61$, which corresponds to a value $\lambda=0.72$. These fits are also shown in Fig. 3.4.3 by dashed lines. At high temperatures, the fits are indistinguishable, but at lower temperatures, they badly reproduce the positions of the minima and deviate unambiguously from the data at frequencies above the susceptibility minima.

These results show that for glycerol, the MCT interpolation formula and β-relaxation scaling law do not describe correctly the experimental data.

c) $(\omega_{min})^{2a}$ and $(\chi''_{min})^2$ versus T plots and determination of T_c.

We made a final test of MCT predictions by checking the linearity in a plot of $(\omega_{min})^{2a}$ and $(\chi''_{min})^2$ versus T. We also tried to estimate T_c from these plots. The values of a and b used were obtained from the constrained fits mentioned in b). The plots are shown in Fig. 3.4.4. For $(\omega_{min})^{2a}$ we found an approximately linear T dependence,

Reproduced with permission of the copyright owner. Further reproduction prohibited without permission.

extrapolating to zero at T_c=225±5K, or ≈ 1.2 T_g [37]. The minima χ''_{min}, however, deviate strongly from the predicted behavior. Finally, if the viscosity data [38] is compared to the MCT prediction $\eta \alpha (T-T_c)^{-\gamma}$ with $\gamma = 1/2a + 1/2b$, the data extrapolate to a much higher $T_c \approx 305$ K [39]. Thus, a consistent T_c could not be obtained.

We summarize the results of this section as follows: The normalized spectra show scaling behavior only over a small frequency range due to deviations from scaling on the high frequency side of the susceptibility minimum. However, the observed limited range scaling does not conform quantitatively to MCT predictions. The determination of T_c, based on relations derived from the scaling laws also fails to give consistent results.

Reproduced with permission of the copyright owner. Further reproduction prohibited without permission.

3.4.3 Discussion

In the previous section we saw how in the intermediate glass former glycerol, the MCT β-relaxation scaling laws fail to describe the light scattering spectra. It has been argued that MCT should not apply to network forming materials (like glycerol), because MCT does not include the dynamics of bond formation and breaking. Also, the strong microscopic structure near 1 THz may perturb the dynamics on the high-frequency side of the minimum, leading to the large values of a found in the free fits. However, the failure of the scaling laws in glycerol does not necessarily mean that MCT can't describe the relaxation dynamics in this material. As was mentioned in section 3.2, the scaling laws are leading order asymptotic results implied by the MCT equations (3.3.2) for temperatures close to T_c and frequencies close to ω_{min}. Experiments with fragile glass formers have shown that these leading order results are appropriate for their description, but, with glycerol, we see that this is not the case, and corrections to scaling may be important.

To improve on the results, it would be necessary to go back to the original MCT Eqs. (3.2.2) and solve them numerically with the vertices evaluated for the intermolecular potential in glycerol. In this way, the solutions would not be limited to temperatures close to T_c or frequencies close to the susceptibility minimum. To solve the equations, the coupling constants must be calculated. These constants can be found from the intermolecular potentials. As mentioned in section 3.2, this has been done for hard sphere [3] and Lennard Jones [29] systems. For real systems like glycerol, the intermolecular potentials are not known. To simplify the calculations, schematic

Reproduced with permission of the copyright owner. Further reproduction prohibited without permission.

models like the ones mentioned in section 3.2, can be used with the coupling constants treated as fitting parameters.

Following this spirit, Franosch, Goetze, Mayr and Singh [40], have reanalyzed our data. They used a two correlator schematic model. One of the correlators, $\phi(t)$, is assumed to describe the density fluctuations and the other, $\phi_s(t)$, is supposed to describe the probing variable (e.g., orientational dynamics). Both correlators satisfy individually Eq. 3.2.2a, but differ in the form of the memory function. For the density fluctuations, the memory function is taken as the F_{12} model of Eq. 3.2.5. The probing variable memory function is proportional to the product of the two correlators. Thus, the liquid-glass transition arises from the density fluctuation correlator ϕ, while the dynamics of ϕ_s are modified via the bilinear interaction with ϕ.

$$m(t) = v^{(1)}\,\phi(t) + v^{(2)}\,\phi^2(t) \qquad (3.2.5)$$

$$m_s(t) = v_s\,\phi(t)\,\phi_s(t) \qquad (3.4.3.1)$$

This model was previously introduced by Sjoegren [41] to describe the tagged particle correlator of a liquid. It has the peculiarity that the first correlator, $\phi(t)$, influences the dynamics of the second, but not vice versa.

In Fig. 3.4.5 we reproduce the MCT fits of the probing variable susceptibility obtained by Franosch et al [40] to our data. As we see, the agreement is remarkable. Notice the large temperature and frequency ranges used. These results show that the

Reproduced with permission of the copyright owner. Further reproduction prohibited without permission.

failure of MCT scaling laws in glycerol was not due to the inapplicability of MCT to this intermediate glass former. Instead, they imply that the leading order MCT formulae are inadequate to describe the dynamics in glycerol.

We also want to make some remarks about the relation between the schematic model used by Franosch et al and the dynamics in glycerol. First, we note that as suggested by Cummins et al [19], the origin of the depolarized light scattering from largely anisotropic molecules like glycerol should be mainly due to orientational fluctuations, which in dense fluids, should couple strongly to density fluctuations [16]. Having this background, we can make the natural association of the density correlator $\phi(t)$, with the density fluctuations in glycerol, and the probing variable correlator $\phi_s(t)$, with the orientational fluctuations. In this way, we have the picture of light scattering spectra in glycerol mainly originating from orientational fluctuations, which in turn, are influenced by (coupled to) the dynamics of the density fluctuations.

These results show that MCT for the liquid to glass transition can also be successfully applied to an intermediate glass former even though the theory was not originally intended for such systems.

Reproduced with permission of the copyright owner. Further reproduction prohibited without permission.

3.4.4 Conclusions

We performed these experiments in glycerol with the goal of finding if the success of MCT with fragile glass formers could be extended to intermediate glasses. Our results have demonstrated that, at least for the intermediate glass former glycerol, the leading order formulae specified by the scaling laws present discrepancies with the data. However, as Franosch et al have shown, a full numerical solution of the MCT equations, even using a simple schematic model, is able to describe our data very well. Thus, we conclude that MCT can also describe the dynamics of intermediate glass forming materials. This is a very important result, which should motivate similar tests with other intermediate and even strong glass formers as has been done with fragile materials. More fundamentally, the results suggest that the MCT for the liquid to glass transition addresses the most relevant processes for the dynamics of viscoelastic fluids.

Reproduced with permission of the copyright owner. Further reproduction prohibited without permission.

4. Low-Frequency Light Scattering Spectroscopy of Powders

4.1. Introduction

Several light-scattering studies of powders have been reported previously [42,43,44,45,46], primarily intended to investigate optical phonons in materials for which large single crystals were not available, or to explore polariton effects in the small size limit. These experiments measured inelastic scattering at frequencies in the Raman scattering region above 10 cm^{-1}. Light scattering spectra of powders have not previously been studied at lower frequencies, primarily because the strong elastic scattering characteristic of powders tends to overwhelm the inelastic scattering at frequencies below ~ 3 cm^{-1}.

Such low-frequency spectra are of considerable interest, however, particularly in biologically active materials such as lysozyme for which a low-frequency intramolecular mode (the "hinge-bending mode") related to enzymatic activity has been predicted [47,48] to occur at a frequency of a few cm^{-1}, but has not yet been observed. It is also of interest to investigate acoustic modes in small particles, which requires extending measurements to the Brillouin scattering region below 1 cm^{-1}. The Sandercock tandem Fabry-Perot interferometer [49] can provide a contrast above 10^{10} in this range, permitting the study of weak inelastic scattering despite the presence of strong elastic scattering. Therefore a Sandercock tandem interferometer has been employed to study the light-scattering spectra of powders in this frequency range.

Reproduced with permission of the copyright owner. Further reproduction prohibited without permission.

4.2. Experiments and results

Light scattering spectra of powders were obtained with incident 488 nm light from a single mode argon laser. Light scattered at 90° to the incident beam was analyzed with a Sandercock tandem Fabry-Perot interferometer operated in 6-pass geometry with mirror separations between 0.4 and 20 mm, covering the spectral range 0.20 to 10 cm^{-1}. With the incident light polarized perpendicular to the scattering plane (V), spectra with the scattered light polarized parallel to (VH) or perpendicular to (VV) the scattering plane were indistinguishable, so spectra were recorded without a polarization analyzer (VV + VH) to increase the available signal intensity.

Initially, we studied the light scattering spectrum of a lyophilized lysozyme powder in a search for the predicted low-frequency hinge-bending mode. The lysozyme spectrum exhibited an unusual band with intensity that increased smoothly with increasing frequency, ending in a sharp cutoff at ~ 0.67 cm^{-1} as shown in Fig. 4.2.1. For frequencies above this cut-off up to 10 cm^{-1}, no additional modes were observed. Similar bands were observed in the spectra of two other enzymes (RNASE and DNASE), suggesting a possible connection with the predicted low-frequency intramolecular vibrational modes. However, the spectra of both organic and inorganic materials (including powdered salol, NaCl, and glass), for which optic modes are not present in this frequency range, were subsequently found to exhibit similar bands (see Fig. 4.2.1), indicating that this band is a universal feature of the light-scattering spectra of powders of transparent materials. Since optic modes are not involved, the spectra are due to scattering from acoustic modes, i.e. Brillouin scattering, as we shall show.

Reproduced with permission of the copyright owner. Further reproduction prohibited without permission.

To explore the relation of this band to the usual Brillouin scattering spectrum of single crystals which contain individual narrow components, a single crystal of salol was ground to successively finer powder, until a fine powder was obtained with an average particle size of ~ 20 μm. As seen in Fig. 4.2.2, the spectrum evolves with decreasing particle size from the discrete components typical of single crystals (a) to the broad band typical of powders (c).

In Fig. 4.2.3 we show the spectrum of powdered glass (a) and of a bulk sample of the same glass (b) at $\beta = 90^{o}$. [In (c) the 90^{o} spectrum in (b) has been scaled in frequency by $\sin(180^{o}/2)/\sin(90^{o}/2)$ to show the expected positions of the LA Brillouin components for $\beta = 180°$.] The longitudinal (LA) Brillouin peak in (c) is seen to coincide with the high-frequency cutoff of the powder spectrum. The observed sharp cutoff of the band at a frequency equal to the maximum allowed Brillouin frequency shift (corresponding to a scattering angle of 180°), together with the evolution of the salol spectra in Fig. 4.2.2 from discrete components to a continuous band provides strong evidence that the band is a result of a distribution of Brillouin lines generated by light scattered at all angles from 0° to 180°.

Reproduced with permission of the copyright owner. Further reproduction prohibited without permission.

4.3 Model for Brillouin scattering from powders.

In this section, we give an explanation to the experimental results presented above. First a simplified version is derived which contains the core of the assumptions of the model, then a more complete theory is introduced which includes the details neglected in the simplified theory.

In a powder, light can be elastically scattered repeatedly from the particle-air interface, producing the typical strong elastic scattering (commonly exploited, e.g., in the covering properties of paint). After 0, 1, 2 or more such elastic scattering events, light may be inelastically scattered from an acoustic mode in a powder particle, producing a Brillouin shift. Since light is incident on any given particle from many different directions (because of multiple elastic scattering), the observed scattered spectrum will be characteristic of a uniform distribution of scattering angles, rather than the single angle characteristic of scattering from a bulk sample. Since from Eq.(2.7.2) the largest Brillouin shift corresponds to $\beta = 180^{o}$, the high-frequency cutoff of the band should correspond to the Brillouin components in 180^{o} scattering from a bulk sample as shown in Fig. 4.2.3. Multiple elastic scattering also explains the observed polarization independence of the spectrum noted in section 4.2. We note that the inelastic scattering cross section is sufficiently small that multiple inelastic scattering need not be considered.

a). Simplified Theory. We first formulate a simplified theory of the scattered spectrum for an isotropic material such as powdered glass (see Fig 4.2.3), for which

Reproduced with permission of the copyright owner. Further reproduction prohibited without permission.

the transverse (TA) modes produce much weaker scattering than the longitudinal (LA) modes and can therefore be neglected. We also ignore any possible dependence of the scattered intensity on scattering angle or on the polarization of the light incident on the particle. The scattering geometry is illustrated in Fig. 4.3.1. The wavevector $\mathbf{k_s}$ of the scattered light is taken as the z-axis of the isotropic powder particle. Light incident on the particle, with wavevector $\mathbf{k_0}$, is assumed to arrive with equal probability from all directions and with all polarizations. The scattering vector $\mathbf{q} = \mathbf{k_s} - \mathbf{k_0}$ (corresponding to anti-Stokes scattering) defines the polar angles θ and ϕ with respect to the particle's axes as indicated in the figure.

The differential scattered intensity produced by light incident in the solid angle element $d\Omega$ will therefore be proportional to $d\Omega$ due to the uniform angular probability of $\mathbf{k_o}$.

$$\delta I(\beta, \phi) \propto d\Omega = \sin\beta \, d\beta \, d\phi \qquad (4.3.1)$$

Due to the assumed isotropy of the medium, the angle ϕ is irrelevant here (although it would be relevant in anisotropic materials where directions must be specified with respect to the crystal axes). We can therefore integrate Eq. (4.3.1) over ϕ, which gives $\delta I(\beta) \propto \sin\beta \, d\beta$, or

$$\delta I(\beta)/d\beta \propto \sin\beta = 2\sin(\beta/2)\cos(\beta/2) \qquad (4.3.2)$$

Reproduced with permission of the copyright owner. Further reproduction prohibited without permission.

The scattered intensity spectrum is $I(\omega) = \delta I/d\omega = (\delta I/d\beta)(d\beta/d\omega)$. From Eq.(2.7.2) it follows that $d\beta/d\omega \propto 1 / \cos(\beta/2)$. Using this expression for $d\beta/d\omega$ and Eq. (4.3.2) in the expression for $I(\omega)$ above gives:

$I(\omega) \propto [\sin(\beta/2)\cos(\beta/2)][1/\cos(\beta/2)] = \sin(\beta/2)$

But from Eq. (2.7.2) again we see that $\sin(\beta/2) \propto \omega$. We then finally have:

$$I(\omega) = B\omega \qquad (4.3.3)$$

where the proportionality factor B can be treated as an adjustable fitting parameter which includes the instrumental response. Equation (4.3.3) predicts a spectrum $I(\omega)$ that increases linearly with frequency from $\omega=0$ up to the maximum $\omega_{max}= (4\pi nv/\lambda_o)$, corresponding to $\beta=180^o$. Note that the spectrum predicted by Eq. (4.3.3) is not changed by additional elastic scattering events subsequent to the Brillouin scattering.

In Fig. 4.3.2 we show the result predicted by this simple model (with an added constant background) superimposed on the observed spectrum of powdered glass. While the qualitative behavior is correct, the predicted shape of the band is evidently wrong.

b). Full Theory. To improve on the result obtained with the simplified approach in a, we must take account of the dependence of scattered intensity on scattering angle and polarization. As in a, we continue to assume that (1) the material is isotropic, (2) the transverse (TA) modes can be ignored, and (3) the light arriving at a given particle is

Reproduced with permission of the copyright owner. Further reproduction prohibited without permission.

isotropic, i.e. all directions of $\mathbf{k_0}$ are equally probable, and it has no preferred polarization. (Assumptions (1) and (2) can be relaxed at the expense of a somewhat more elaborate calculation.). We then apply the procedure described in chapter 2 to calculate the scattering intensity.

For simplicity in the derivation, **q** is taken in the x-z plane with ϕ=0 (see Fig.4.3.1). The result will again be independent of ϕ due to the assumed isotropy. Then **q** and the local material displacement **u** of the LA mode will be:

$$\mathbf{q} = q\,(\sin\theta\ \hat{x} + \cos\theta\ \hat{z})$$

$$\mathbf{u} = u\,(\sin\theta\ \hat{x} + \cos\theta\ \hat{z}) \qquad (4.3.4)$$

so: $\hat{q}_x = \hat{u}_x = \sin\theta$, $\hat{q}_y = \hat{u}_y$ and $\hat{q}_z = \hat{u}_z = \cos\theta$

From Eq. (2.7.4), the 6 component strain x_n is then:

$$x_1 = q\,u\,(\sin^2\theta)$$

$$x_2 = 0$$

$$x_3 = q\,u\,(\cos^2\theta)$$

$$x_4 = 0$$

$$x_5 = 2\,q\,u\,\sin\theta\,\cos\theta$$

$$x_6 = 0 \qquad (4.3.5)$$

Reproduced with permission of the copyright owner. Further reproduction prohibited without permission.

The Pockels tensor for an isotropic material has the form:

$$p_{nm} = \begin{bmatrix} p_{11} & p_{12} & p_{12} & 0 & 0 & 0 \\ p_{12} & p_{11} & p_{12} & 0 & 0 & 0 \\ p_{12} & p_{12} & p_{11} & 0 & 0 & 0 \\ 0 & 0 & 0 & p_{44} & 0 & 0 \\ 0 & 0 & 0 & 0 & p_{44} & 0 \\ 0 & 0 & 0 & 0 & 0 & p_{44} \end{bmatrix} \qquad (4.3.6)$$

where $p_{44} = (p_{11} - p_{12}) / 2$

The 6-component reciprocal dielectric constant ΔB_m from Eq. (2.7.5) gives:

$$\Delta B_1 = qu (p_{11} \sin^2 \theta + p_{12} \cos^2 \theta)$$

$$\Delta B_2 = qu\, p_{12}$$

$$\Delta B_3 = qu (p_{12} \sin^2 \theta + p_{11} \cos^2 \theta)$$

$$\Delta B_4 = 0$$

$$\Delta B_5 = qu (p_{11} - p_{12}) \sin \theta \cos \theta$$

$$\Delta B_6 = 0$$

These ΔB_m are converted to a 3 x 3 tensor ΔB_{nm} using Eq. (2.7.6) which gives:

$$\Delta B_{11} = q\, u\, (p_{11} \sin^2\theta + p_{12} \cos^2\theta)$$

$$\Delta B_{22} = q\, u\, p_{12}$$

Reproduced with permission of the copyright owner. Further reproduction prohibited without permission.

$$\Delta B_{33} = q\,u\,(p_{12}\sin^2\theta + p_{11}\cos^2\theta)$$

$$\Delta B_{13} = \Delta B_{31} = q\,u\,(p_{11} - p_{12})(\sin\theta\cos\theta)$$

$$\Delta B_{12} = \Delta B_{21} = \Delta B_{23} = \Delta B_{32} = 0 \qquad (4.3.7)$$

Then, from Eqs. (2.7.7) and (4.3.7) we find for the scattering tensor T:

$$T = n^4 \begin{bmatrix} (p_{11}\sin^2\theta + p_{12}\cos^2\theta) & 0 & (p_{11} - p_{12})\sin\theta\cos\theta \\ 0 & p_{12} & 0 \\ (p_{11} - p_{12})\sin\theta\cos\theta & 0 & (p_{12}\sin^2\theta + p_{11}\cos^2\theta) \end{bmatrix} \qquad (4.3.8)$$

From Fig. 4.3.1, with ϕ=0, the unit polarization vectors are:

$$\begin{array}{llll} \hat{e}_0: & \hat{y} \quad (V); & \hat{x}\cos\beta + \hat{z}\sin\beta & (H) \\ \hat{e}_s: & \hat{y} \quad (V); & \hat{x} & (H) \end{array} \qquad (4.3.9)$$

The four scattered intensities are, from Eqs. (2.7.3), (4.3.8) and (4.3.9), therefore:

$$\begin{array}{ll} \text{VV:} & I \propto p_{12}^2 \\ \text{VH:} & I = 0 \\ \text{HV:} & I=0 \\ \text{HH:} & I \propto [(p_{11}\sin^2\theta + p_{12}\cos^2\theta)\cos\beta + (p_{11}-p_{12})\sin\theta\cos\theta\sin\beta]^2 . \end{array} \qquad (4.3.10)$$

Reproduced with permission of the copyright owner. Further reproduction prohibited without permission.

With the assumption of isotropic polarization of the light incident on the particle in which the Brillouin scattering takes place, the unpolarized scattered intensity I is proportional to the sum of the terms in Eq. (4.3.10).

Similar to Eq.(4.3.1) for the simplified case, we then have

$$\delta I \propto f(\beta)\, d\Omega = f(\beta) \sin\beta\, d\beta\, d\phi \qquad (4.3.11)$$

where the function $f(\beta)$, which is not present in Eq.(4.3.1), is:

$$f(\beta) = \{ p_{12}^2 + [(p_{11} \sin^2\theta + p_{12} \cos^2\theta) \cos\beta + ((p_{11} - p_{12}) \sin\theta \cos\theta) \sin\beta]^2 \} \qquad (4.3.12)$$

Then, following the same procedure as in a) to get $I(\omega)$ we have:

$$\delta I(\beta)/d\beta \propto f(\beta) \sin\beta = 2 f(\beta) \sin(\beta/2) \cos(\beta/2),$$

$$d\beta/d\omega \propto 1 / \cos(\beta/2)$$

and $I(\omega) \equiv \delta I/d\omega = (\delta I/d\beta)(d\beta/d\omega)$ gives:

$$I(\omega) \propto \omega f(\beta) \qquad (4.3.13)$$

If we define a quantity A as:

$$A = p_{11} / p_{12} \qquad (4.3.14)$$

Reproduced with permission of the copyright owner. Further reproduction prohibited without permission.

then Eq. (4.3.12) can be written as:

$$f(\beta) = p_{12}^2\{ 1 + [(A \sin^2\theta + \cos^2\theta) \cos\beta + ((A - 1) \sin\theta \cos\theta) \sin\beta]^2 \}$$

and the scattering intensity will be:

$$I(\omega) = B\, \omega \{ 1 + [(A \sin^2\theta + \cos^2\theta) \cos\beta + ((A - 1) \sin\theta \cos\theta) \sin\beta]^2 \} \qquad (4.3.15)$$

where B as in part a) can be treated as an adjustable fitting parameter which includes the instrumental response.

The ratio p_{11}/p_{12} can be evaluated in terms of the intensity and velocity of the LA mode (in VV scattering) and the TA mode (in VH scattering), obtained by performing a 90° scattering experiment on a bulk sample as explained below.

From Eq. (4.3.10) we see that $I_L(VV)$ including the v_L dependence from Eq.(2.7.3) is:

$$I_L(VV) \alpha (1/v_L^2)\, p_{12}^2 \qquad (4.3.16)$$

Reproduced with permission of the copyright owner. Further reproduction prohibited without permission.

To get I_T (VH) we can take advantage of the isotropy of the material and get the Brillouin scattering tensors already tabulated in [20] for q in the x direction . Then the TA mode with $\hat{u}$ in the y direction is characterized by the tensor:

$$T = n^4 \begin{bmatrix} 0 & \frac{p_{11}-p_{12}}{2} & 0 \\ \frac{p_{11}-p_{12}}{2} & 0 & 0 \\ 0 & 0 & 0 \end{bmatrix} \qquad (4.3.17)$$

If scattering takes place in the xz plane, the unit polarization vectors for 90° VH scattering are $\hat{e}_o = \hat{y}$ and $\hat{e}_s = \frac{\sqrt{2}}{2}(\hat{x},-\hat{z})$, then using Eq. (2.7.3) we get :

$$I_T\,(VH) = (1/v_T^2)\,(\,p_{11}^2 - p_{12}^2\,)\,/\,8 \qquad (4.3.18)$$

A similar calculation of I_T for the other TA mode (the one with $\hat{u}$ along the z direction) using the corresponding T tensor also tabulated in (10) gives $I_T = 0$; so, the total intensity of the TA mode from a 90°, VH scattering experiment is given by Eq.(4.3.18) above. From Eqs. (4.3.16) and (4.3.18) we then have:

Reproduced with permission of the copyright owner. Further reproduction prohibited without permission.

$$\frac{I_{LA}(VV)}{I_{TA}(VH)} = \frac{v_T^2}{v_L^2} \cdot \frac{8\,p_{12}^2}{(p_{11}-p_{12})^2} \qquad (4.3.19)$$

from where:

$$A = \frac{p_{11}}{p_{12}} = 1 \pm \sqrt{8}\,\frac{v_T}{v_L}\left(\frac{I_{TA}(VH)}{I_{LA}(VV)}\right)^{1/2} \qquad (4.3.20)$$

To decide which root to take in Eq.(4.3.20), we first measured v_T / v_L and I_T / I_L:

$$v_T / v_L = \omega_T / \omega_L = 0.59$$

where we have used $\omega = q\,v$ for long wavelength acoustic phonons.

The intensity ratio was determined using peak intensities since the Brillouin lines had no measurable linewidth above the instrumental width and gave the value:

$$I_T / I_L = 0.11$$

Substitution in Eq. (4.3.20) gives for the two roots the values:

$A_+ = 1.54$ and $A_- = 0.46$

Reproduced with permission of the copyright owner. Further reproduction prohibited without permission.

We then searched the value p_{11}/p_{12} for silica glass reported in [50] and found p_{11}/p_{12}=0.45. This indicated that the negative root $A_- = 0.46$ was the correct one and used it in our calculations.

Reproduced with permission of the copyright owner. Further reproduction prohibited without permission.

4.4. Comparison with experiment

To compare Eq. (4.3.15) to light scattering data, θ is converted to β as $\theta = (180°-\beta)/2$ (see Fig. 4.3.1) and β is then converted to ω via Eq. (2.7.2):

$$\beta = 2 \sin^{-1}[\omega\lambda_0/4\pi nv] \qquad (4.4.1)$$

The value $\lambda_0/4\pi nv = 3.0 \times 10^{-11}$ s/rad in the argument of (4.4.1) is determined experimentally by using Eq.(2.7.2) with $\beta = 90°$ and the Brillouin frequency shift ω corresponding to the LA mode.

We compared the powdered glass spectrum shown in Fig. 4.4.1 to the theoretical prediction of Eq. (4.3.15). In the comparison, we added a constant background C=74, to Eq.(4.3.15), the intensity measured at $\omega \geq 3.7 \times 10^{10}$ Hz which is beyond the range of the observed Brillouin band. We tried to determine the value of C by measuring the instrumental response with a small portion of the laser beam directed into the collection optics. The instrumental response was essentially flat for frequencies $\geq 1.3 \times 10^{10}$ Hz from the laser line, with a level of $\sim 1.4 \times 10^{-10}$ relative to the laser line peak at $\omega = 0$. For frequencies below 1.3×10^{10} Hz the background increases rapidly with decreasing ω.

The central part of the spectrum in Fig.4.4.1 was attenuated by 2×10^9, so that the elastic scattering at $\omega = 0$ is $600 \times 2 \times 10^9$. The estimated background would then have the value: $(1.4 \times 10^{-10}) \times (600 \times 2 \times 10^9) \sim 170$, which is about twice the actual

Reproduced with permission of the copyright owner. Further reproduction prohibited without permission.

signal at the minima near $\omega = \pm 3.7 \times 10^{10}$ Hz. This difference is presumably due to slightly different illumination of the interferometer in the two measurements.

The fit shown in Fig. 4.4.1 was limited exclusively to the region between 2×10^{10} and 3.26×10^{10} Hz. At frequencies near and below 2×10^{10} Hz the spectrum is distorted by both the TA mode distribution and the frequency-dependent background due to the strong elastic scattering. This is why the theoretical curve falls below the data at the low frequency end. The fit obtained is clearly superior to the simplified theory predictions.

Reproduced with permission of the copyright owner. Further reproduction prohibited without permission.

4.5. Conclusions

The low-frequency light scattering spectra of transparent powders exhibit a characteristic broad band with a high-frequency cutoff. The band is a universal feature of powders which results from Brillouin scattering corresponding to scattering at all angles from 0° to 180° due to multiple reflections and refractions. The frequency of the cutoff can be used to estimate the longitudinal sound velocity. The presence of this band will inevitably complicate the search for weak low frequency vibrational modes lying below the upper limit of 180° Brillouin scattering. However, for frequencies above this upper limit (e.g., for glass, above 36 GHz), the tandem Fabry-Perot can be used to study weak spectral features in the presence of intense elastic scattering.

Reproduced with permission of the copyright owner. Further reproduction prohibited without permission.

5. CONFORMATIONAL CHANGES IN PEPTIDES

5.1 Introduction.

This chapter describes an infrared spectroscopic study of synthesized peptides. This is in order to explore the possibility of enhancement of their helical structure by formation of intramolecular hydrogen bonds. These bonds are expected to be formed between carboxylic groups in the side chains of different glutamic acid amino acid residues. Circular dichroism (CD) measurements, conducted by Prof. Baldwin's research group at Stanford University, have suggested such interactions can stabilize the helix (personal communication). We must note that this is different from the main helix formation mechanism whereby the hydrogen bonding takes place between atoms in the backbone of the polypeptide chain. This such research is important for the better understanding of secondary structure formation in proteins. More fundamentally, secondary structure formation is essential for the overall process of protein folding, by which proteins achieve their biologically active folded state.

The rest of the chapter is organized as follows: In section 5.2 we describe the samples, preparation techniques, and experimental equipment. Section 5.3 contains the results of the infrared absorption measurements and subsequent data analysis. Section 5.4 is devoted to the discussion of the experimental results. We end the chapter with conclusions supporting the possibility of the side chains H-bond helical-enhancement interaction.

Reproduced with permission of the copyright owner. Further reproduction prohibited without permission.

5.2 Materials and experiments.

The peptides were prepared in the laboratory of Prof. Baldwin at Stanford University. The amino acid sequence of each of them is

Peptide	Sequence	# of residues
ae6i3	Ac-AAEAAEAAEAAEAAEAAEAAGY-NH_2	22 residues
ae6i4	Ac-EAAAEAAAEAAAEAAAEAAAEGY-NH_2	23 residues
ae6i2,5	Ac-EAAAAEAEAAAAEAEAAAAEGY-NH_2	22 residues

where A stands for alanine, E for glutamic acid, G for glycine and Y for tyrosine amino acid residues. Ac means the acid terminal of the peptide chain. The peptides synthesizing procedure may have left some residual trifluoracetic acid (TFA). This acid has bands in the region of interest for our experiments and should be removed from the samples. In order to eliminate the TFA, peptide ae6i2,5 was passed through a Sephadex G10, medium gel in a column, 4 cm long and 0.7 cm in diameter. The collected sample had a concentration about 3 times smaller than the one before filtration. The reference buffer solution was also collected from the same column. For the other two peptides, instead of column filtration we used lyophilizations in D_2O, about 40 hours for each peptide. This procedure should also eliminate TFA because it

Reproduced with permission of the copyright owner. Further reproduction prohibited without permission.

has a much smaller molecular weight than the peptides. The advantage of this procedure is that much less sample is wasted compared to the case of column filtration.

The peptides were dissolved in D_2O at a salt concentration of 10 mM NaCl. The pH was adjusted to the desired values by addition of the proper amounts of DCl and NaOD as needed. The acid and base used were also at 10 mM NaCl. In all cases we began preparing the sample at the highest pH, then lowered it monotonically through the other desired values. This sequence was followed in order to help prevent aggregation that occurs at low pH. The concentrations used with the peptides were 1.15 mg/ml for ae6i4, 1.25 mg/ml for ae6i3, and 2.1 mg/ml for ae6i2,5. All concentrations were determined spectro-photometrically in a Perkin Elmer lambda 3B UV/VIS spectrophotometer using the tyrosine UV absorbance at 276 nm.

The sample solution and buffer reference were loaded into calcium fluoride infrared cells for spectroscopic measurements at temperatures around 5 ^{0}C in a BRUKER IFS 66 Fourier Transform Infrared Spectrometer. Both sample and reference buffer were prepared in D_2O instead of H_2O to avoid the strong water absorption bands in the spectral region of interest.

5.3 Experimental results and data processing.

The IR spectra normalized to equal amplitude of the amide I band are shown in Figs.5.1-3. This normalization of intensities via the amide I band was an approximation

Reproduced with permission of the copyright owner. Further reproduction prohibited without permission.

to an equal concentration normalization. The intensity of the amide I band changes at most 10% for a full transition between a helical to a random coil peptide and in our case we expect only a relatively small increase in the helicity. Consequently, in our case the intensity of the amide-I band should not change by more than about 3% over the melting transition. This procedure was performed because we could not make a spectrophotometric determination of the concentration for each pH used due to the small amount of sample available (about 1 mg).

The spectra for all peptides show the decrease in the intensity of the COO^- symmetric (s) and asymmetric (as) bands at 1407 and 1564 cm^{-1} respectively and the simultaneous increase of the C=O band (at 1707 cm^{-1}) of the carboxylic group of the glutamic acid as the pH decreases. This is a common feature which arises from the deuteration of the carboxylic group.

We can estimate the pKa of the peptides from an spectroscopic derived titration curve. To do this we measure the intensity of a band fully dependent on the ionization state of the sample. In our spectra, the best band for this purpose is the COO^- asymmetric band. If the IR absorption intensity for the band is proportional to the concentration of the ionized species and there is a full transformation from the deuterated to the ionized species as the pH increases (or viceversa if it decreases), then the spectral titration curve can be described by the Hendersen-Hasselbalch equation for the component that increases its abundance with pH,

$$\frac{I}{I_{ref}} = \frac{C}{1+(K_a 10^{pH})^{-1}} \qquad (5.3.1)$$

Reproduced with permission of the copyright owner. Further reproduction prohibited without permission.

where I is the intensity of the COO^- (as) band as a function of the pH, I_{ref} is the intensity of a reference band which does not change with pH, C is the maximum value of I/I_{ref}, and Ka is the acid dissociation constant. If the maximum value of the COO^- asymmetric band is used as reference, then C becomes 1. By fitting the data to Eq.5.3.1, Ka is calculated and pKa=-logKa can be determined.

The values of the intensity were measured by finding the amplitude of the COO^- (as) band after subtraction of a two point baseline tangent to the closest intensity minimum on each side of the peak. We fit our data with Eq. 5.3.1 and obtained pKa values of 5.1 for peptide ae6i4 and 5.9 for ae6i3. These results are shown in Figs. 5.4 and 5.5. For peptide ae6i2,5 this procedure failed because there were only three useful points due to aggregation of the sample at pH 3.0 and 2.1. We also performed a control experiment which consisted in measuring the IR spectra of deuterated acetic acid at different pHs. Using the same procedure we obtained a value of 4.9 for the pKa of D-acetic acid.

We also analyzed the amide I band by measuring its position and generating double differences spectra. The double difference spectra were obtained by subtraction of each spectrum from the spectrum at the highest pH for each peptide. These spectra for peptides ae6i3 and ae6i4 are shown in Figs. 5.6 and 5.7 respectively. In all cases the behavior is similar with a positive difference centered around 1650 cm^{-1} and a negative one around 1620 cm^{-1}. The frequency 1650 cm^{-1} is characteristic of random coil, while 1620 cm^{-1} corresponds to helical structure.

Reproduced with permission of the copyright owner. Further reproduction prohibited without permission.

5.4 Discussion

The pKa of isolated glutamic acid corrected for measurements in D_2O is about 4.5. Our measurements of the peptides show a shift in pKa to higher values: 1.5 units for ae6i3 and 0.6 for ae6i4. The pKa values obtained by Prof. Baldwin's group using CD measurements were 5.8 for ae6i3 and 6.2 for ae6i4, showing again a pKa shift to higher values. The agreement between the pKa obtained from CD and IR is very good for peptide ae6i3 and less good for ae6i4. This shift to a higher pKa indicates that D is more tightly bound to the glutamic acid in the peptide than it is when in an isolated state. This opens the possibility of a stabilizing intramolecular D-bond interaction between different Glu side chains.

Our control experiment with concentrated D-acetic acid gave us a pKa value of 4.9. It is known that carboxylic acids have a strong tendency to be in a dimmeric form linked by hydrogen bonds [51]. We used concentrated acid, so, it is reasonable to assume that the dimeric form was heavily dominant at the low pH values. Therefore, we can take the value of 4.9 as a marker indicating the presence of D-bonds in carboxylic acids. The frequency (1705 cm^{-1}) of the C=0 band in D-acetic acid was found to be coincident within 2 or 3 cm^{-1} with the corresponding band in the peptides. This band is sensitive to the formation of H-bonds and should be around 1745 cm^{-1} when H-bonds are not present. These results support the likelihood of H-bonding among the Glu residues in our systems.

Reproduced with permission of the copyright owner. Further reproduction prohibited without permission.

The double difference spectra in the amide I region indicate the following: The positive differences on the random coil region and the negative differences on the helical region mean that the helical component increases with decreasing pH. This can also be explained by the formation of H-bonds between Glu residues as they deuterate at low pH.

Therefore, the analysis of both the pKa shifts and double differences spectra indicate the possibility of intramolecular D-bonding between side chains of Glu residues leading to an enhancement of the helical propensity of the peptides.

It could be argued that the pKa shift results from intermolecular D-bonding. This seems unlikely because it would not explain the enhancement of the helical component shown in the double differences spectra.

5.5 Conclusions

The correlation between the pKa shift of the peptides to values well above the ones characteristic of the isolated glutamic acid on the one hand, and the enhancement of the helical component with deuteration of the Glu residues shown in the amide-I study on the other, are enough evidence to support the possibility of H-bond linking between carboxylic groups in the side chains of Glu residues. This will be an important indication of side chain H-bond interactions stabilizing a helical structure in addition to the more traditional back-bone interaction.

Reproduced with permission of the copyright owner. Further reproduction prohibited without permission.

Table I: **Frequency and susceptibility at the susceptibility minimum from the light scattering spectrum of glycerol as a function of the temperature.**

T(K)	fmin(GHz)	χ"min
243	**9.38**	**1.0**
253	**18.7**	**1.7**
263	**38.3**	**3.3**
273	**62.6**	**5.3**
293	**107.5**	**9.2**
313	**154.6**	**12.9**

Reproduced with permission of the copyright owner. Further reproduction prohibited without permission.

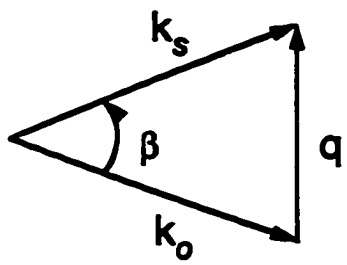

Fig. 2.6.1. Light scattering geometry for the anti-Stokes case. $k_0 \approx k_s$, so, $q = 2k_s\sin(\beta/2)$.

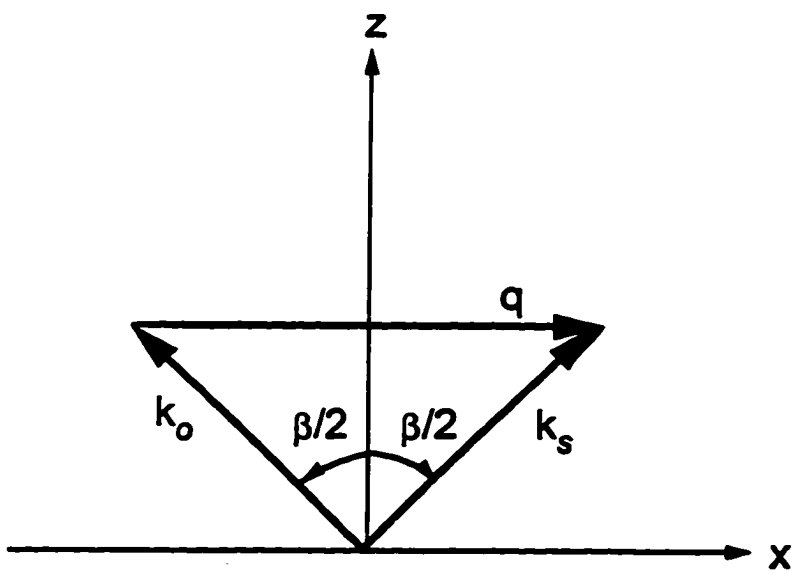

Fig. 2.8.1. Light scattering geometry in the xz plane with q along the x direction

Reproduced with permission of the copyright owner. Further reproduction prohibited without permission.

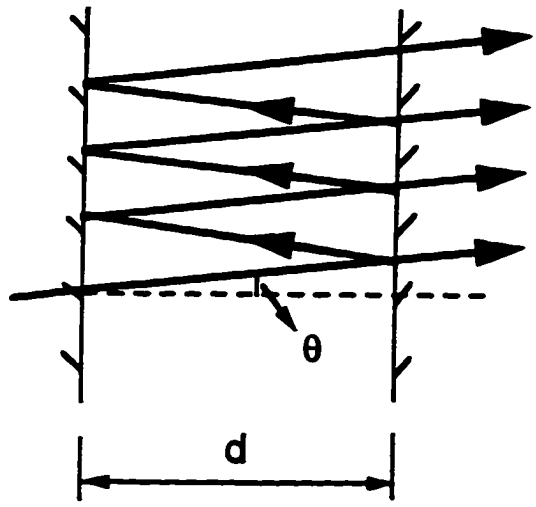

Fig. 2.9.1. Single pass Fabry-Perot. Mirrors are separated by a distance d. Multiple beam interference occurs among all parallel beams forming an angle θ with respect to the axis of the cavity.

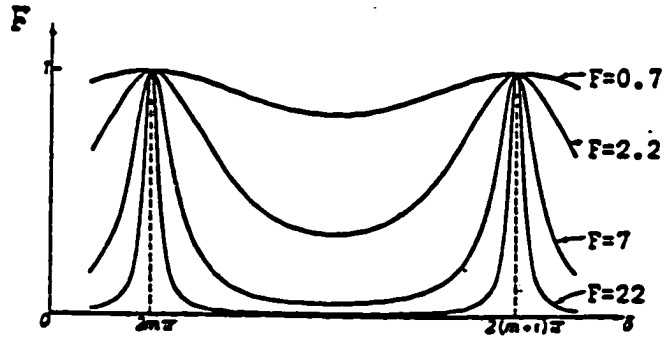

Fig. 2.9.2. Transmission function of the Fabry-Perot vs d (at θ = 0) for several values of the finesse.

Reproduced with permission of the copyright owner. Further reproduction prohibited without permission.

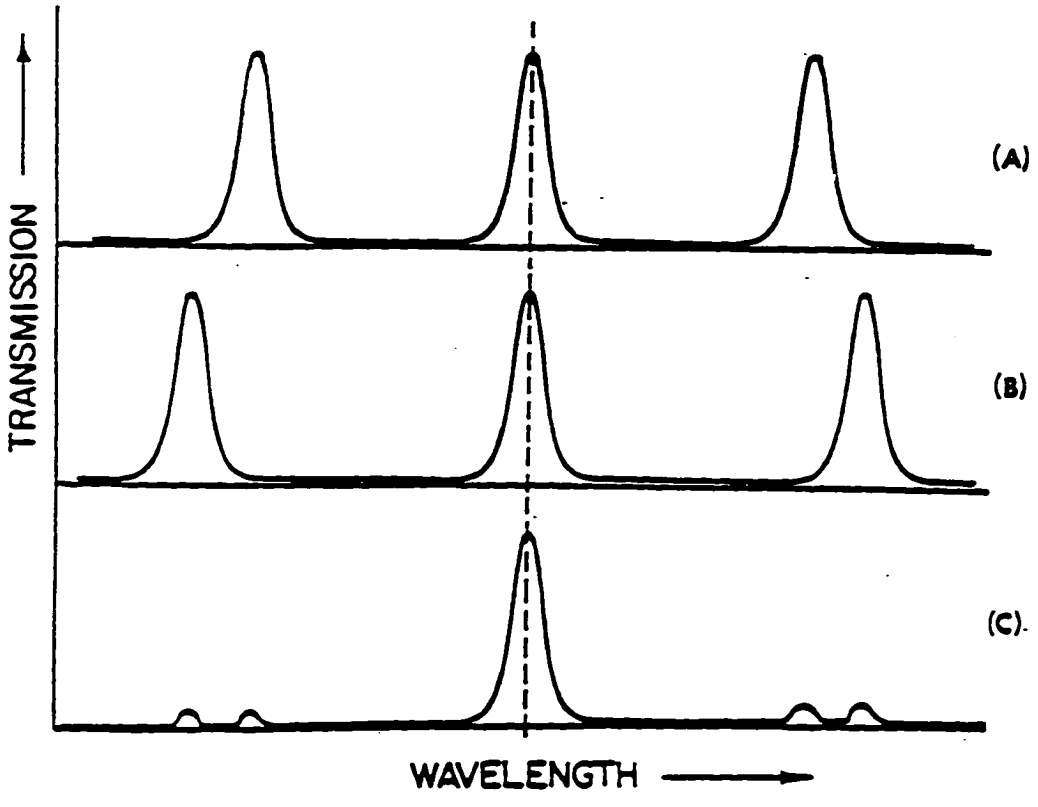

Fig. 2.9.3. Transmission of two cavities of different mirror separations (A and B) and the series transmission of the pair (C).

Reproduced with permission of the copyright owner. Further reproduction prohibited without permission.

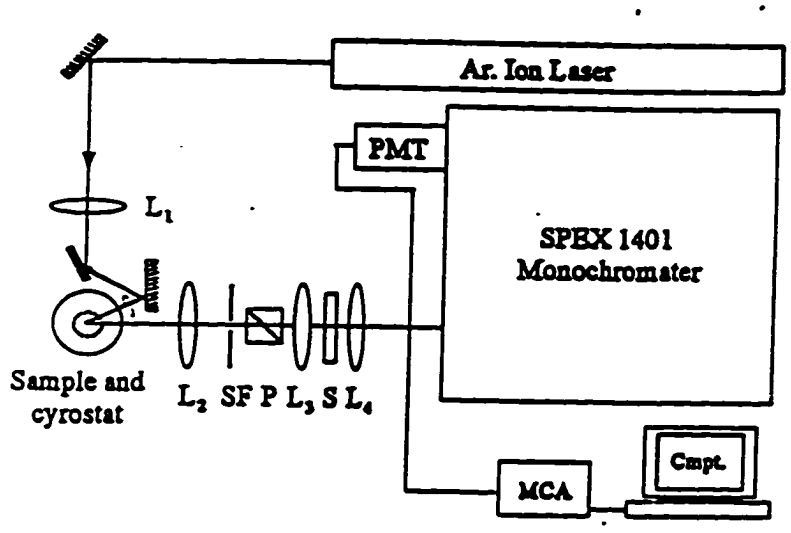

Fig. 2.10.1. Schematic optical layout for Raman scattering spectroscopy.

Reproduced with permission of the copyright owner. Further reproduction prohibited without permission.

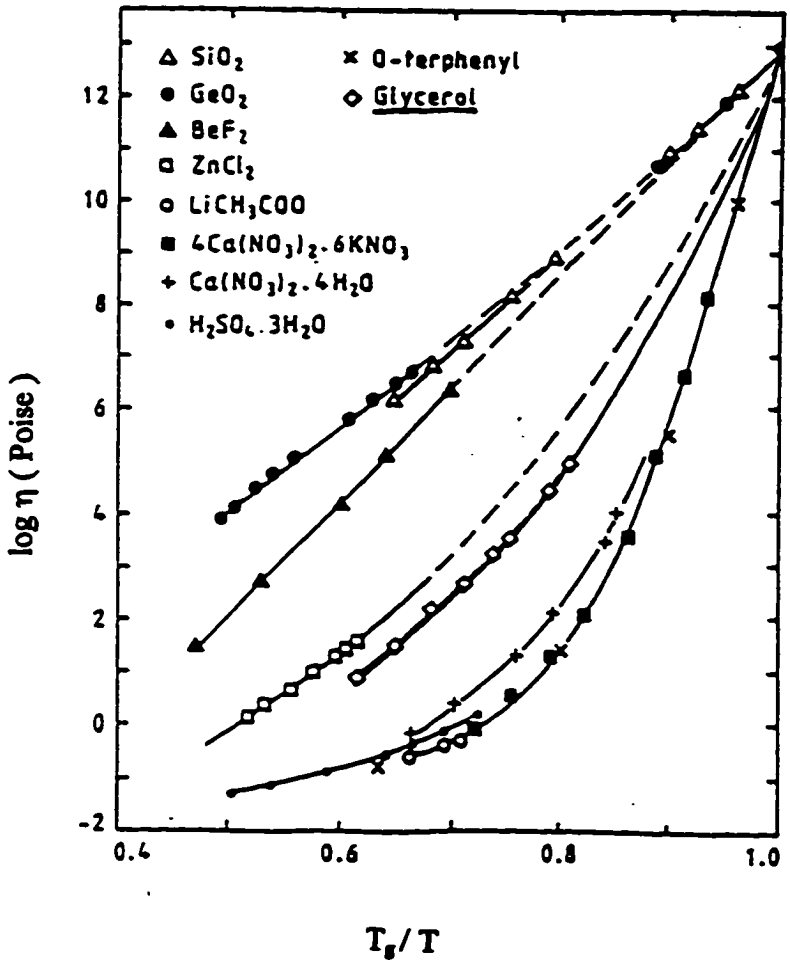

Fig. 3.1.1. Angel plot for the classification of glass forming materials. Strong glass formers: top curves; fragile: bottom curves.

Reproduced with permission of the copyright owner. Further reproduction prohibited without permission.

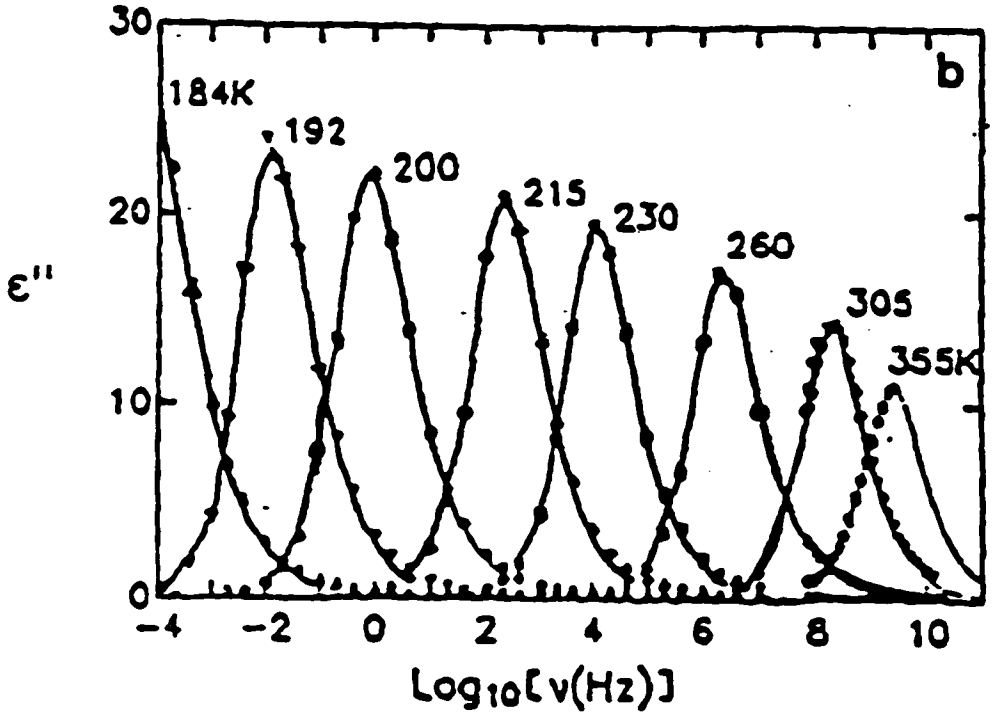

Fig. 3.1.2. Dielectric loss measurements ε" (ω) in glycerol (From [25]).

Reproduced with permission of the copyright owner. Further reproduction prohibited without permission.

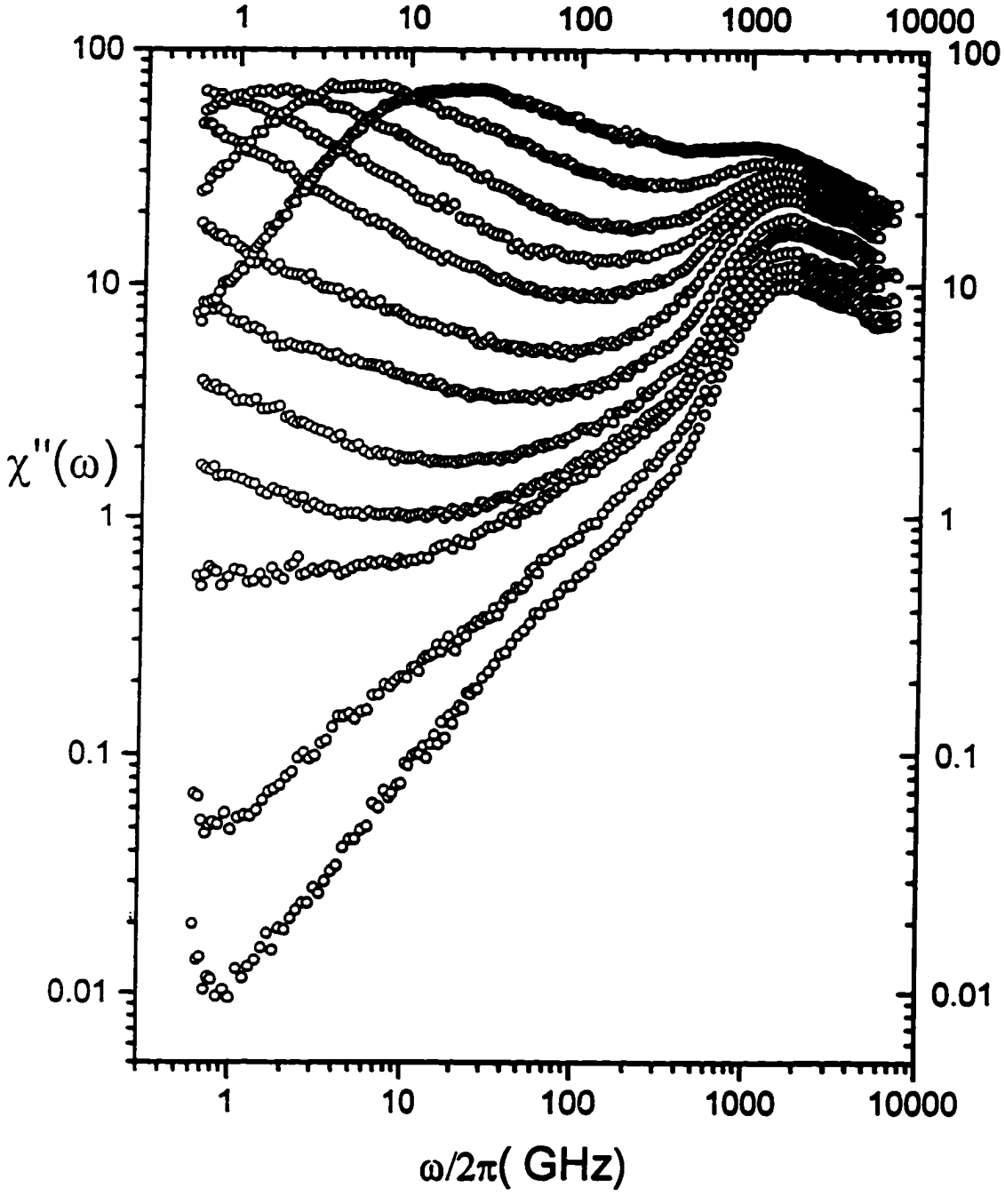

Fig. 3.1.3. Light scattering susceptibility spectra from glycerol

Reproduced with permission of the copyright owner. Further reproduction prohibited without permission.

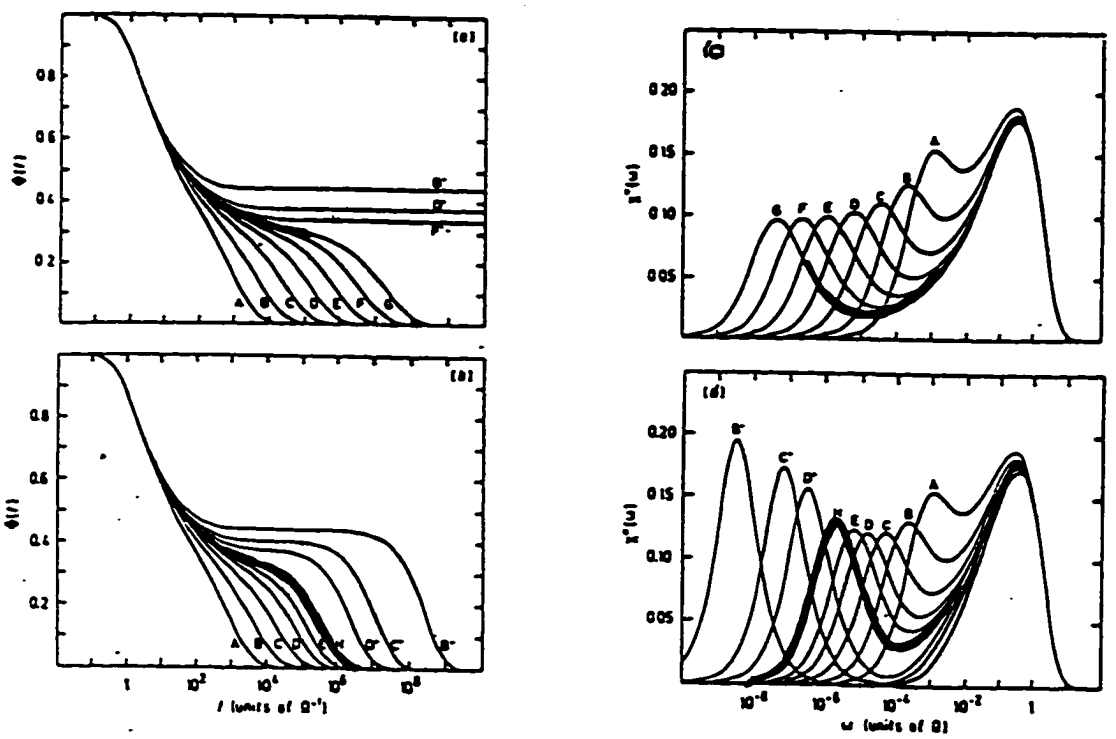

Fig. 3.2.1. **MCT calculated density fluctuations correlation functions and susceptibility spectra for the F_{12} schematic model as a function of the temperature for the idealized (a, c) and extended (b, c) versions of the theory.**

Reproduced with permission of the copyright owner. Further reproduction prohibited without permission.

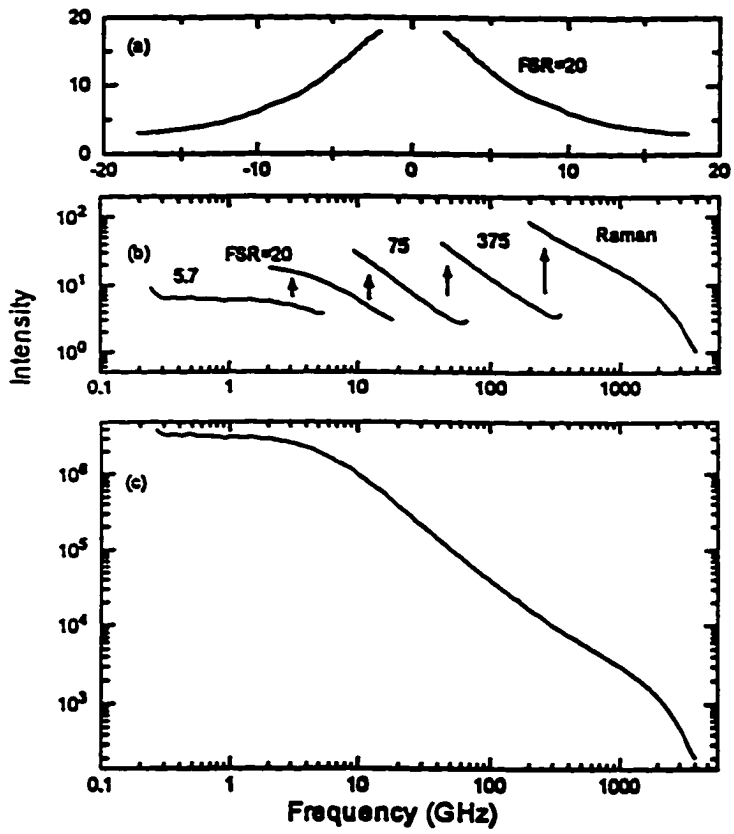

Fig. 3.4.1. Illustration of the splicing procedure of individual spectra at the same T to obtain a composite spectrum over a larger frequency range (reproduced from W. Du, Ph. D. thesis, CUNY, New York 1996).

Reproduced with permission of the copyright owner. Further reproduction prohibited without permission.

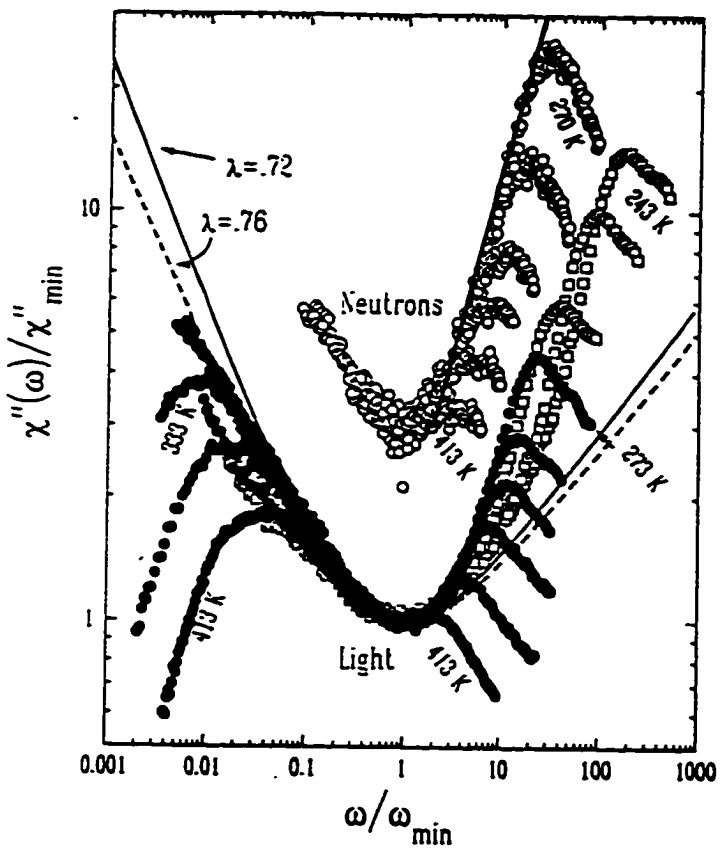

Fig.3.4.2. Susceptibility spectra scaled so that the minima coincide. Neutron scattering data from Wuttke [35] is included for comparison. For clarity, the neutron data are shifted upward by a factor of 3. The solid and broken lines are MCT interpolations for different values of λ. A line of slope 1 is shown through the high-frequency side of the neutron data.

Reproduced with permission of the copyright owner. Further reproduction prohibited without permission.

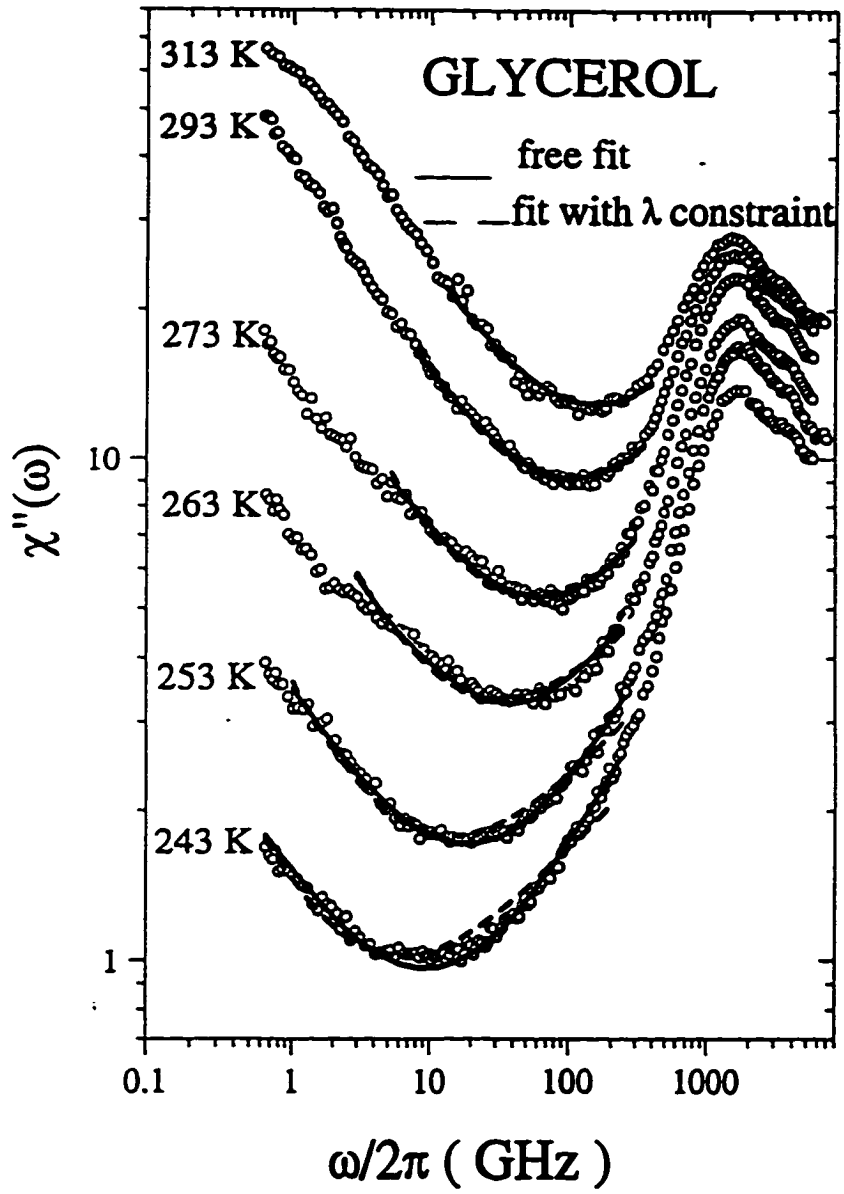

Fig.3.4.3. Light scattering spectra with fits to the MCT interpolation equation. The solid lines are global fits with unconstrained a and b. Free fits: a=0.54, b=0.43. Constrained fits: λ=0.72, a=0.32, b=0.61.

Reproduced with permission of the copyright owner. Further reproduction prohibited without permission.

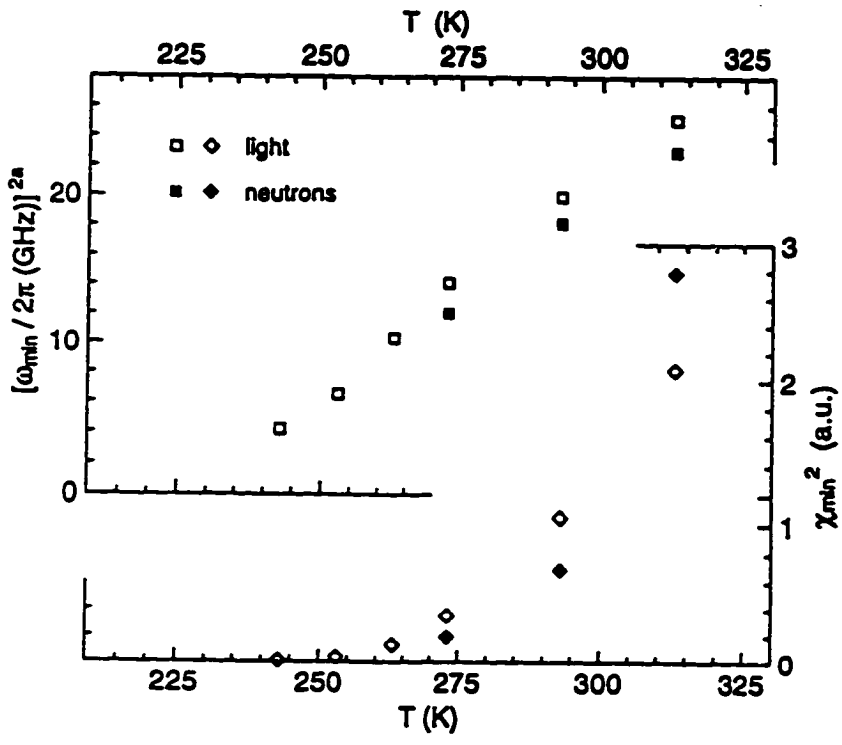

Fig. 3.4.4. (ω_{min})^{2a} (top) and (χ''_{min})^2 (bottom) vs T. Neutron results from Wuttke [35] are included for comparison (with $a_L = 0.32$, $a_N = 0.35$). The ω_{min} and χ''_{min} values were taken from the unconstrained fits.

Reproduced with permission of the copyright owner. Further reproduction prohibited without permission.

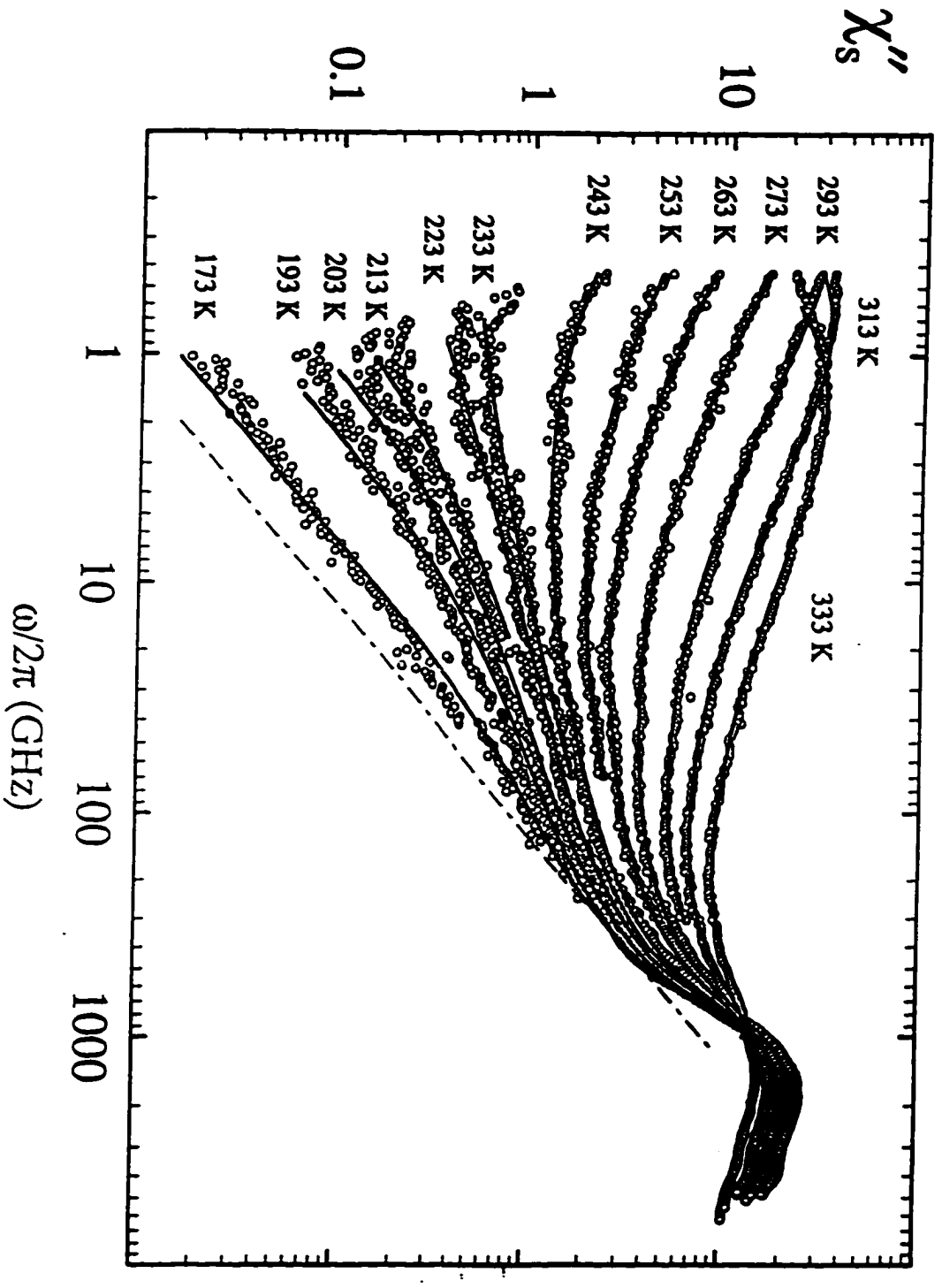

Fig. 3.4.5. Susceptibility spectra from this work, fit by MCT numerical solutions (solid lines) for the model described by Eqs. 3.2.2a, 3.2.5 and 3.4.3.1.(Reproduced from [40])

Reproduced with permission of the copyright owner. Further reproduction prohibited without permission.

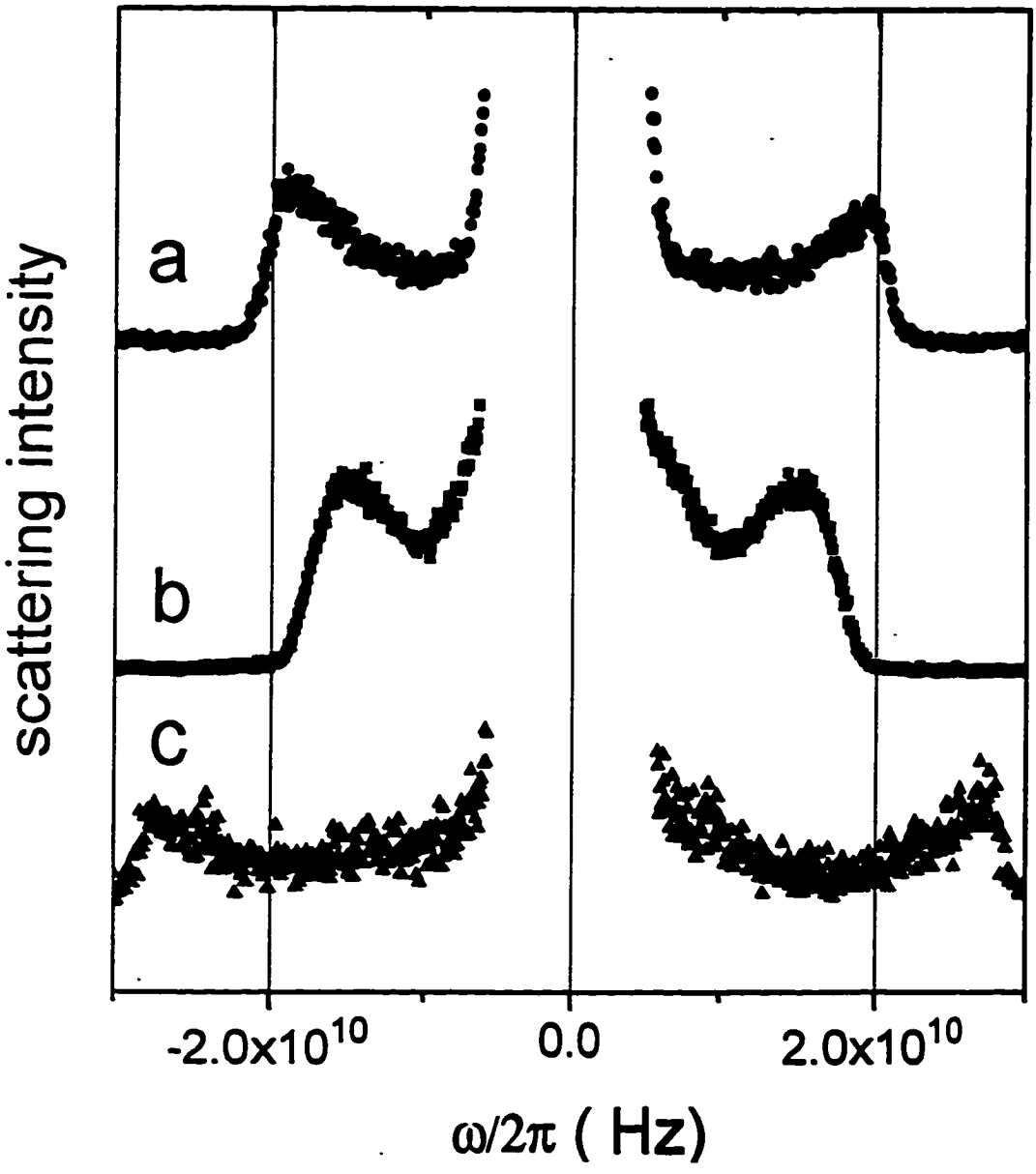

Fig. 4.2.1. Low-frequency light scattering powder spectra of lysozyme (a), salol (b), and NaCl (c) in the range 0 to ±3 x10^{10} Hz (0 to ±1 cm^{-1}), showing the low-frequency band characteristic of powders of transparent materials. The spectra have been shifted vertically for clarity. In this and subsequent figures, the mirror separation is 4 mm, corresponding to a free spectral range of 1.25 cm^{-1} or 3.75 x 10^{10} Hz. The central part of the sample spectrum has been blocked by a shutter.

Reproduced with permission of the copyright owner. Further reproduction prohibited without permission.

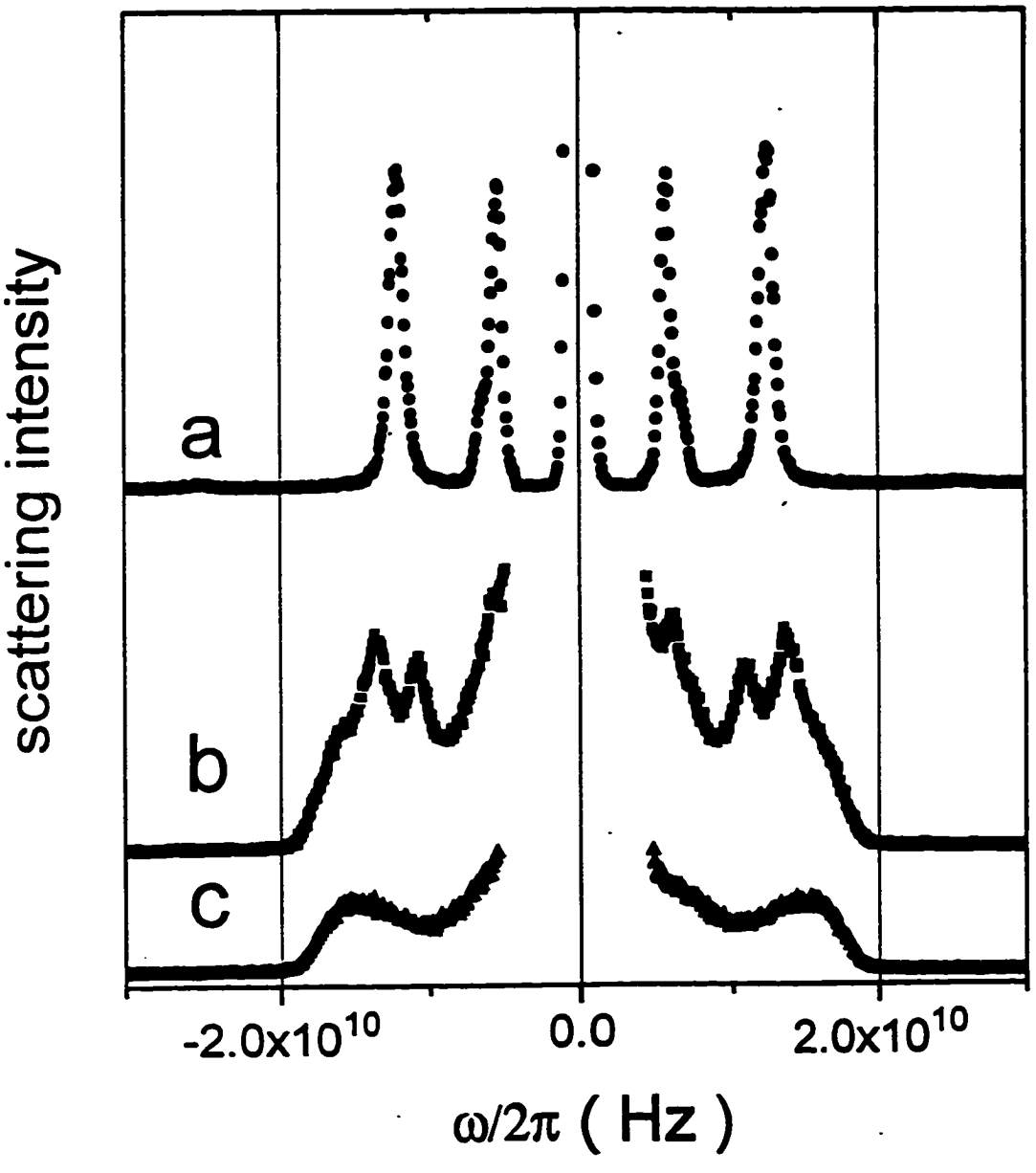

Fig 4.2.2. Evolution of the light-scattering spectrum of salol with decreasing size. (a): bulk crystal, (b) powder with mean particle size ~ 200 μm, (c) powder with mean particle size ~ 20 μm.

Reproduced with permission of the copyright owner. Further reproduction prohibited without permission.

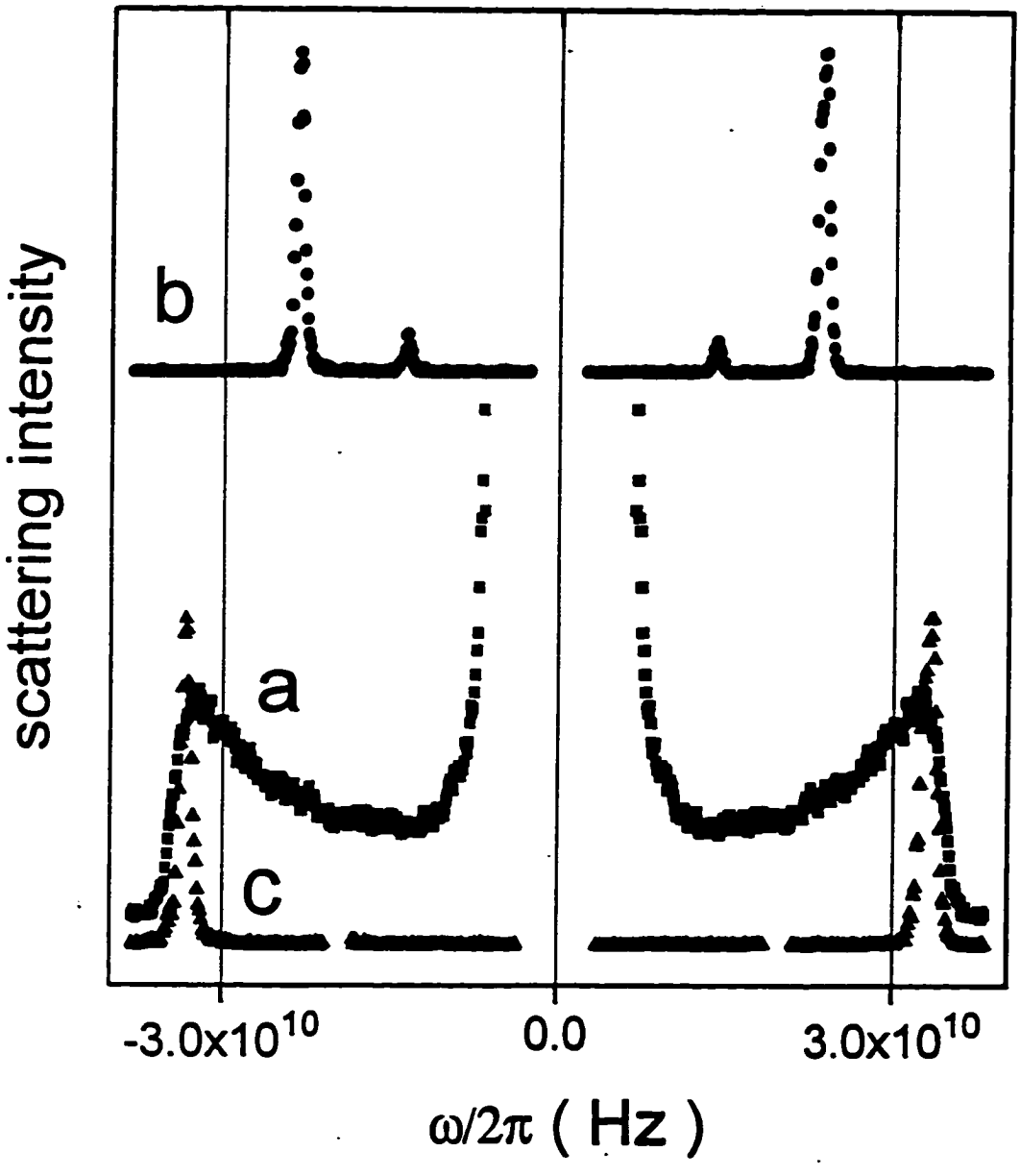

Fig 4.2.3. Low frequency spectra of powdered glass (a) with mean size ~ 30 μm, and bulk glass at (b) $\beta = 90^{o}$. In (c) the LA modes in (b) were frequency scaled by $\sin(180^{o}/2)/\sin(90^{o}/2)$ to indicate the expected positions of the LA modes for $\beta=180^{o}$.

Reproduced with permission of the copyright owner. Further reproduction prohibited without permission.

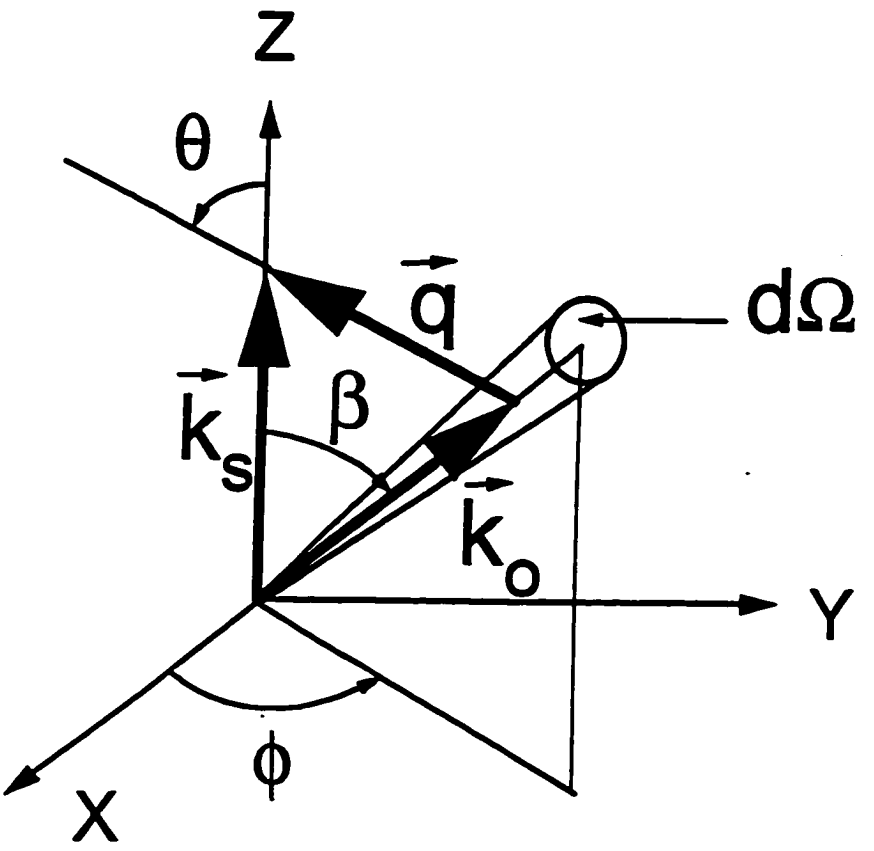

Fig. 4.3.1. Illustration of the scattering geometry. k_s is the wavevector of the scattered light, which also defines the z-axis of the particle. k_0 is the wavevector of the incident light, arriving at the particle either directly or after one or more elastic scattering events. $q = k_s - k_0$ is the (anti-Stokes) scattering vector.

Reproduced with permission of the copyright owner. Further reproduction prohibited without permission.

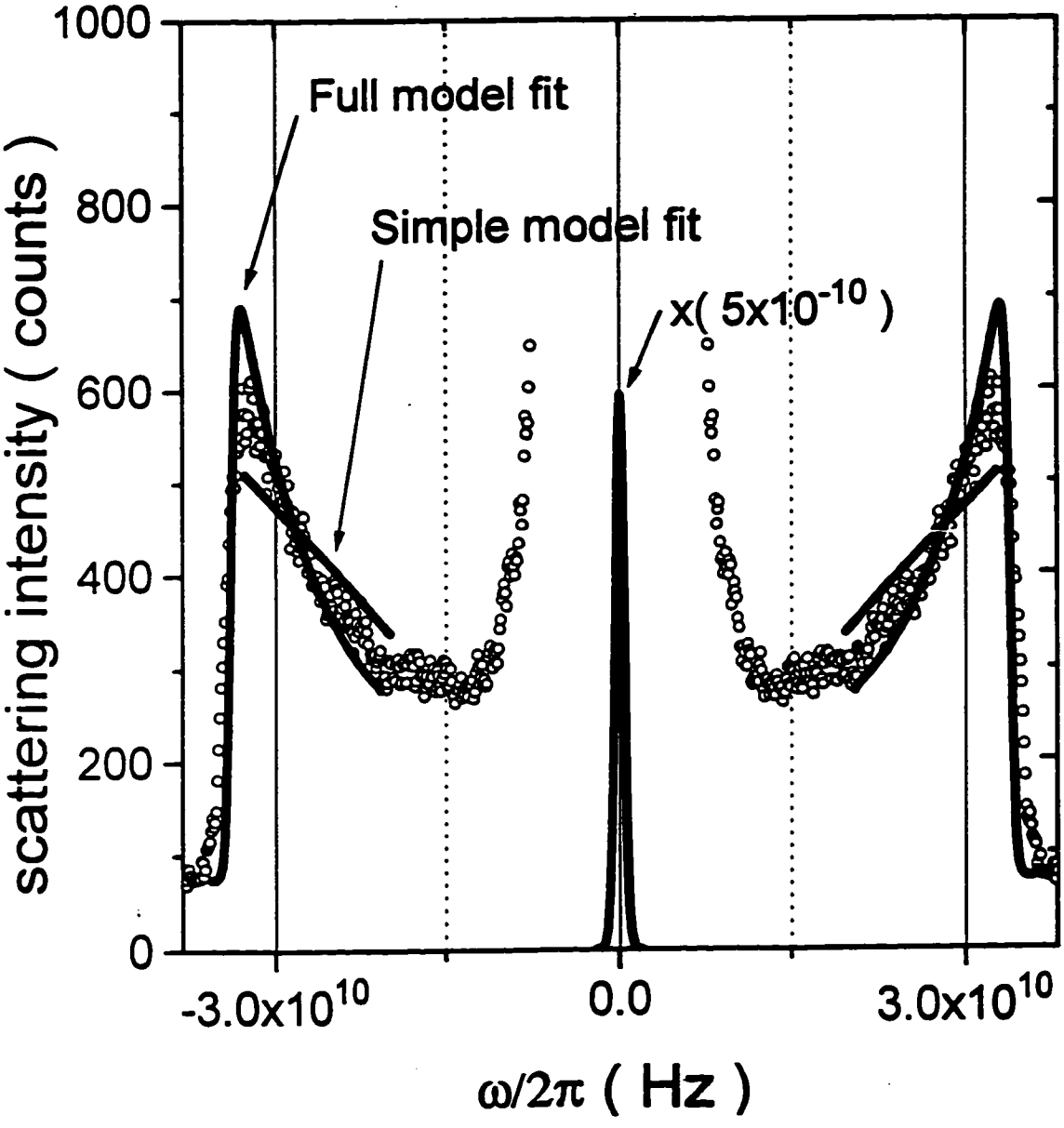

Fig 4.4.1. Comparison of the observed spectrum of powdered glass with the prediction of the simple theory [Eq. (4.3.3)] and the full theory [Eq. (4.3.15)] convoluted with the instrumental function. The theoretical spectra are added to a background as described in the text. The experimental spectrum is an average of the Stokes and the anti-Stokes sections.

Reproduced with permission of the copyright owner. Further reproduction prohibited without permission.

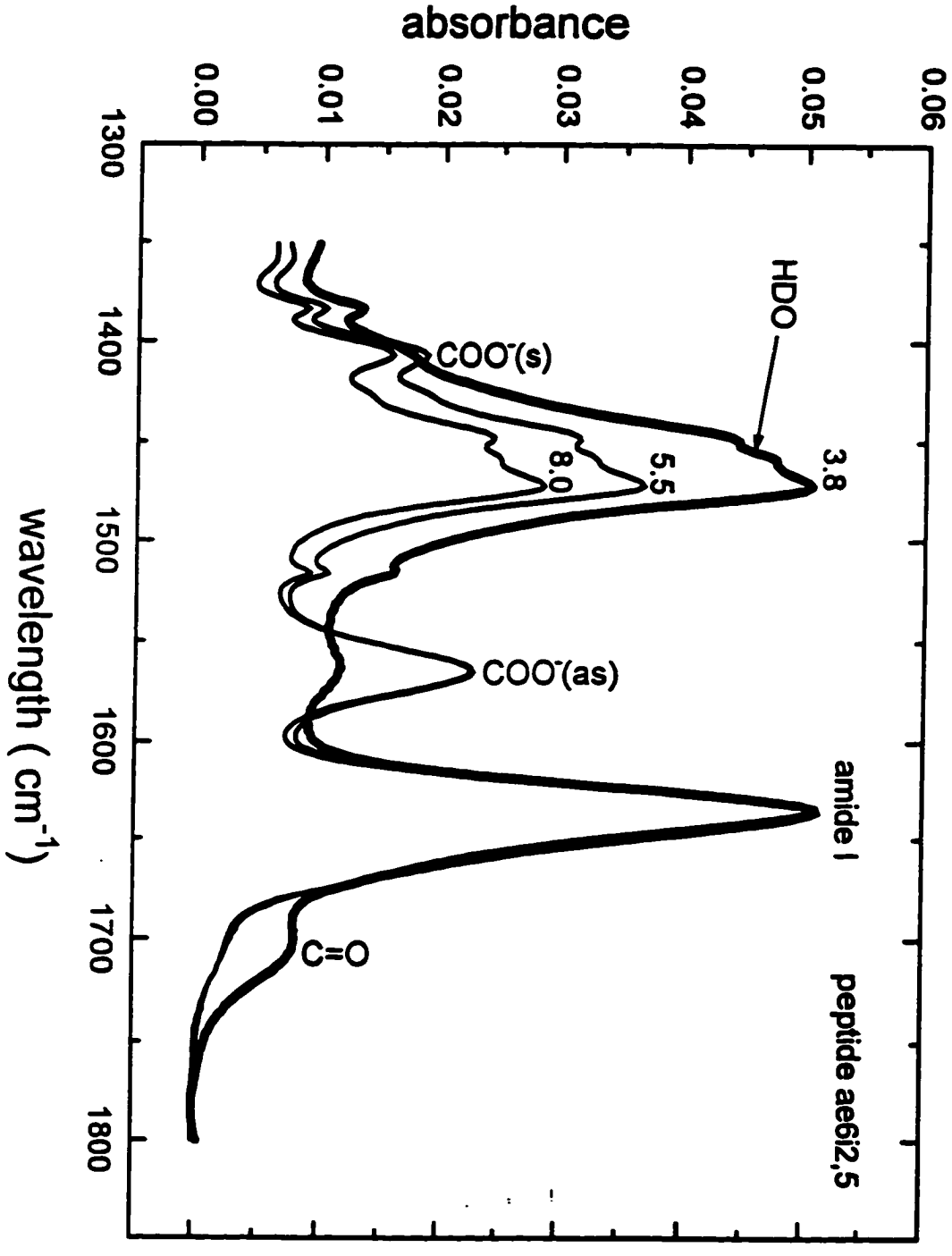

Fig. 5.1 Absorbance spectra of peptide ae6i2,5 normalized at equal amplitude of the amide I band. The pH is indicated on each curve.

Reproduced with permission of the copyright owner. Further reproduction prohibited without permission.

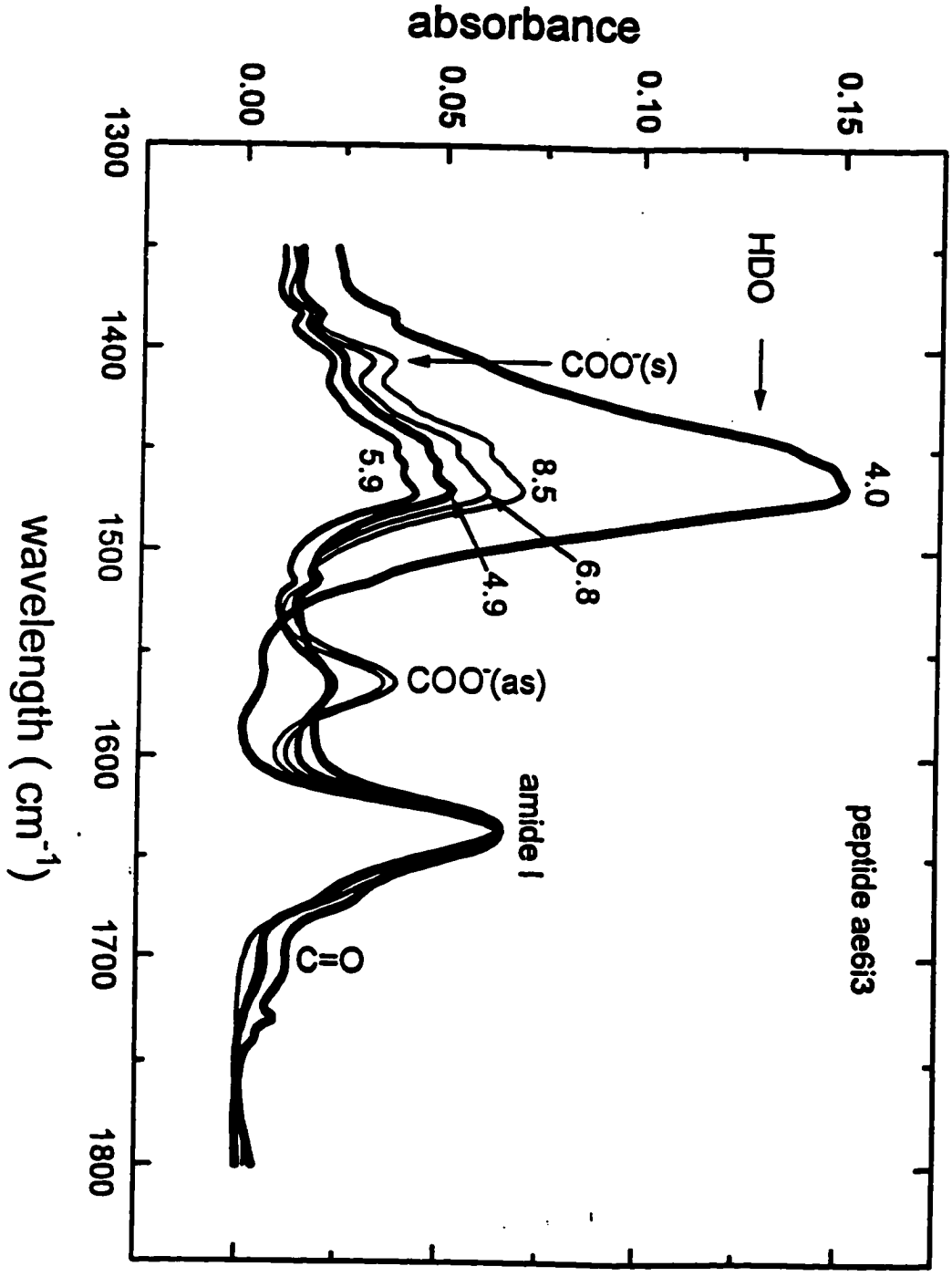

Fig. 5.2 Absorbance spectra of peptide ae6i3 normalized at equal amplitude of the amide I band. The pH is indicated on each curve.

Reproduced with permission of the copyright owner. Further reproduction prohibited without permission.

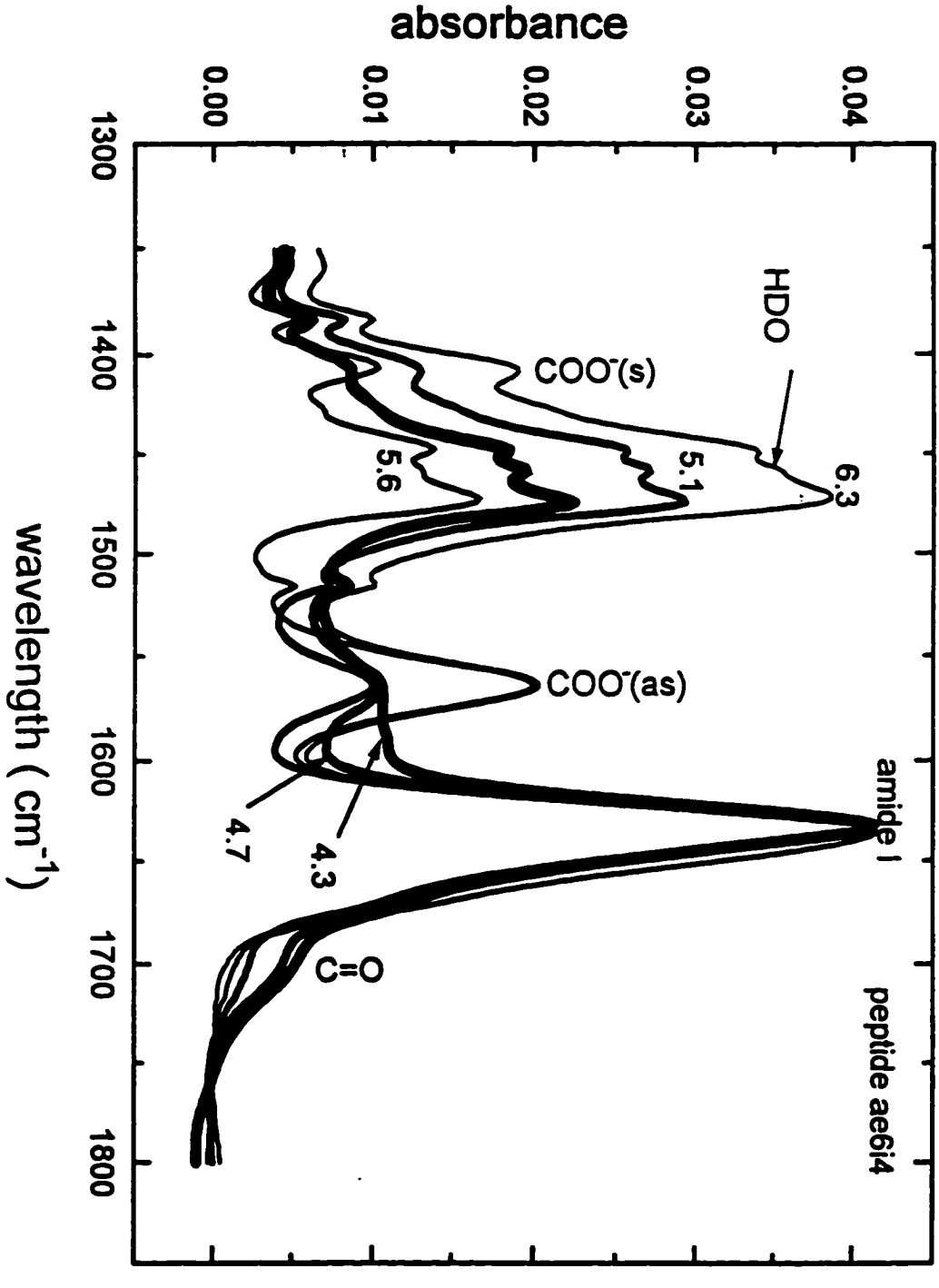

Fig. 5.3 Absorbance spectra of peptide ae6i4 normalized at equal amplitude of the amide I band. The pH is indicated on each curve.

Reproduced with permission of the copyright owner. Further reproduction prohibited without permission.

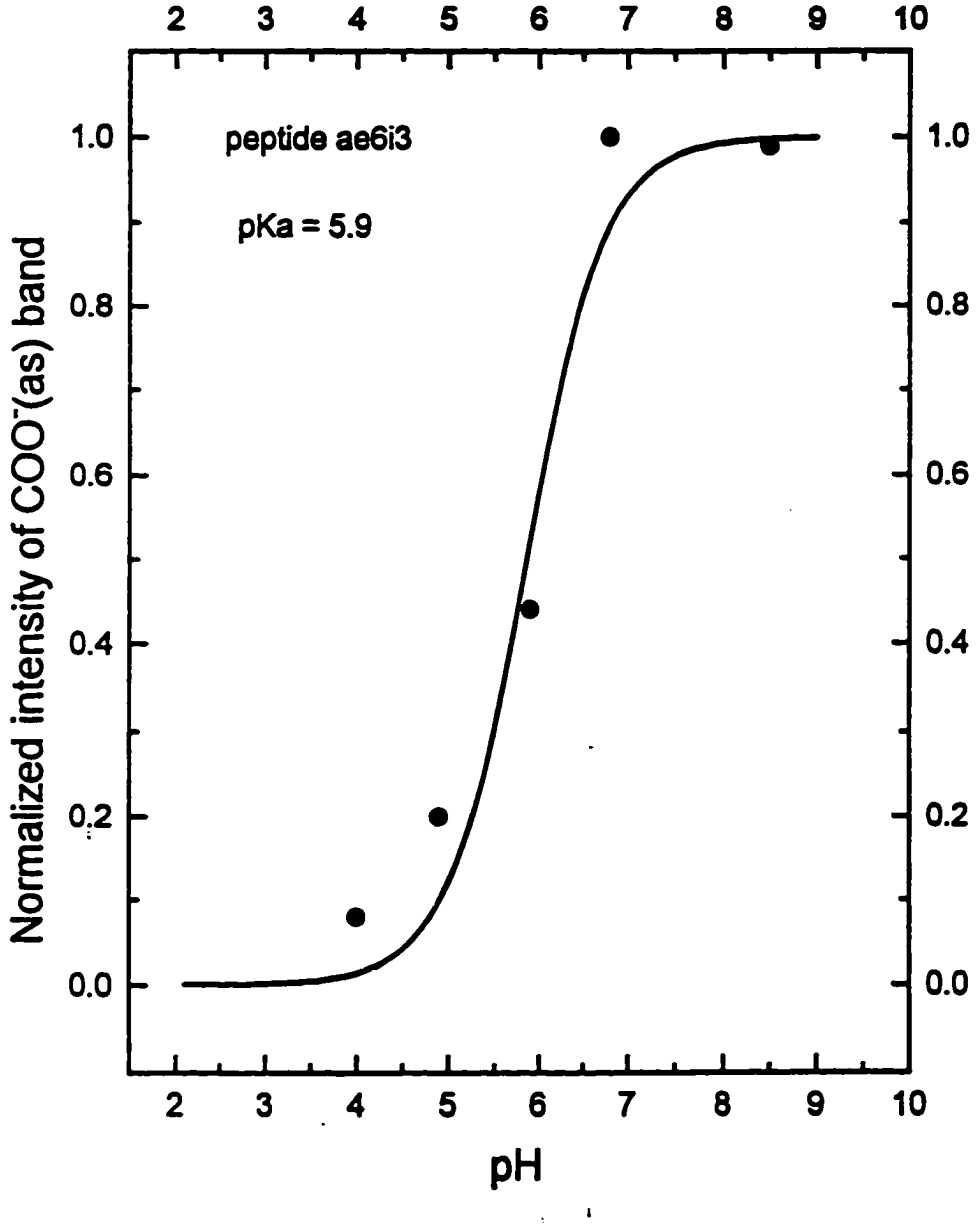

Fig. 5.4 Spectral titration curve for peptide ae6i3. The intensity of the COO^-(as) band has been normalized with respect to its maximum value.

Reproduced with permission of the copyright owner. Further reproduction prohibited without permission.

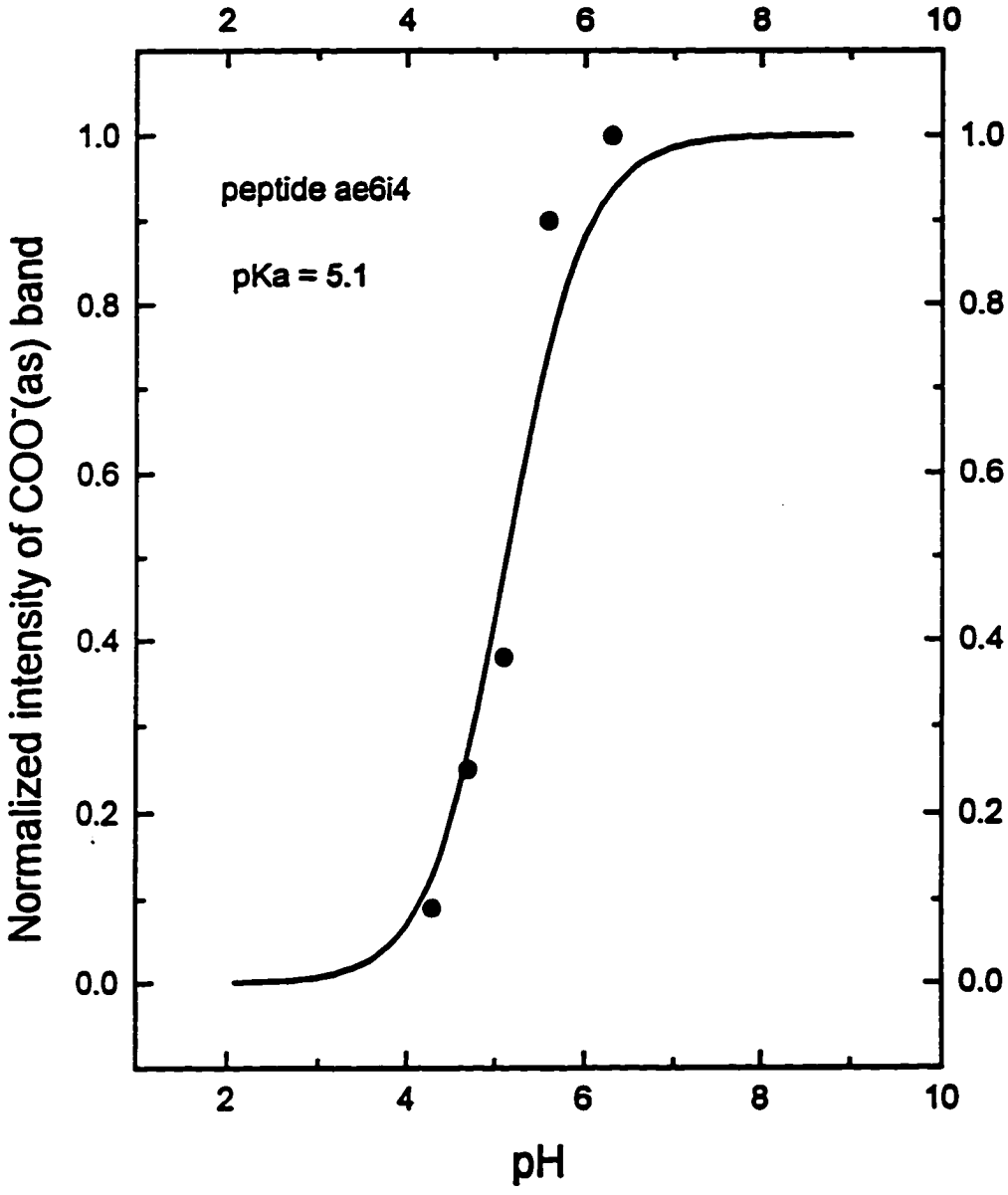

Fig. 5.5 Spectral titration curve for peptide ae6i4. The intensity of the COO^-(as) band has been normalized with respect to its maximum value.

Reproduced with permission of the copyright owner. Further reproduction prohibited without permission.

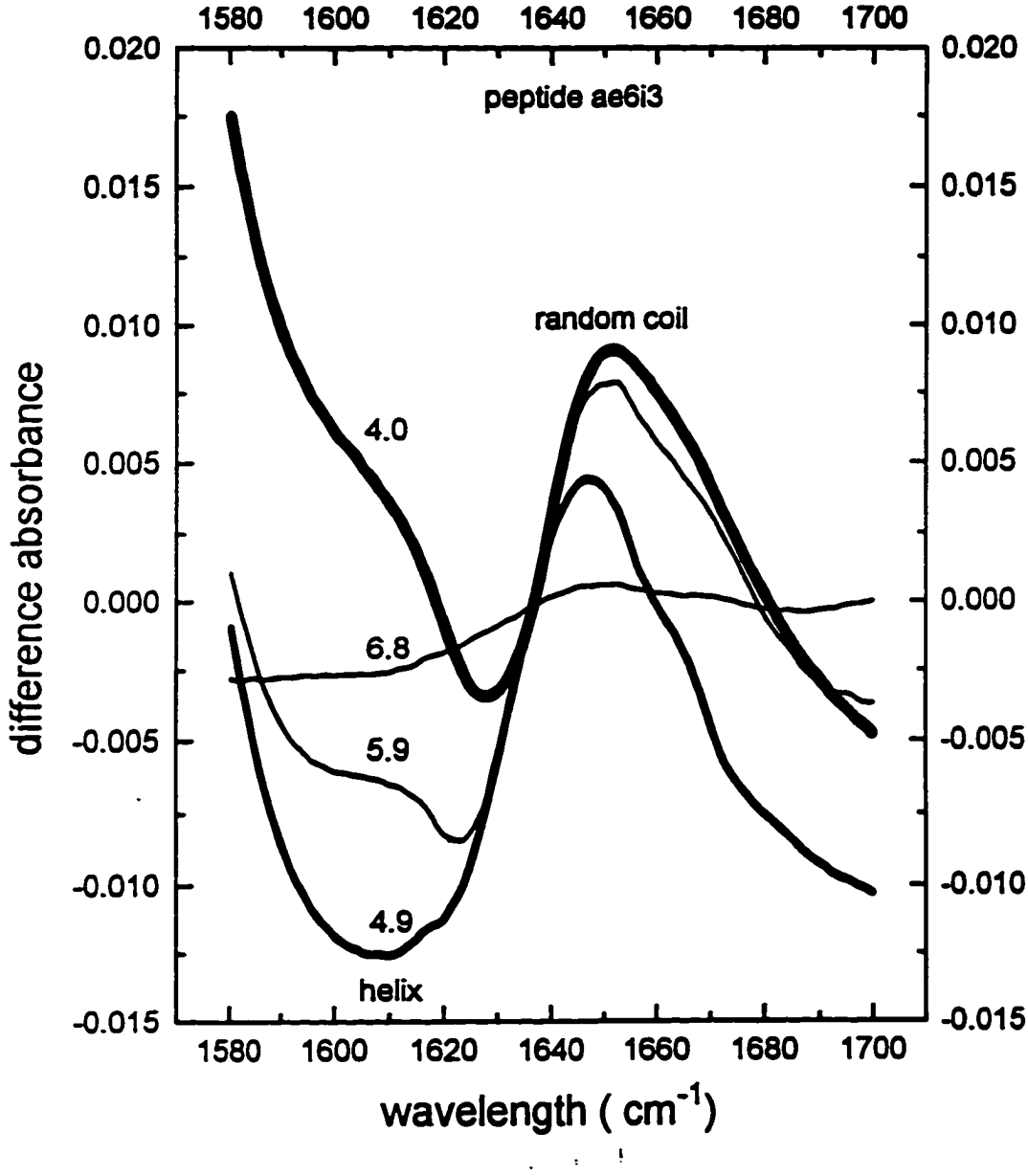

Fig. 5.6 Double differences spectra for peptide ae6i3 in the amide I region. The pH is indicated on each curve. The helical content increases with decreasing pH.

Reproduced with permission of the copyright owner. Further reproduction prohibited without permission.

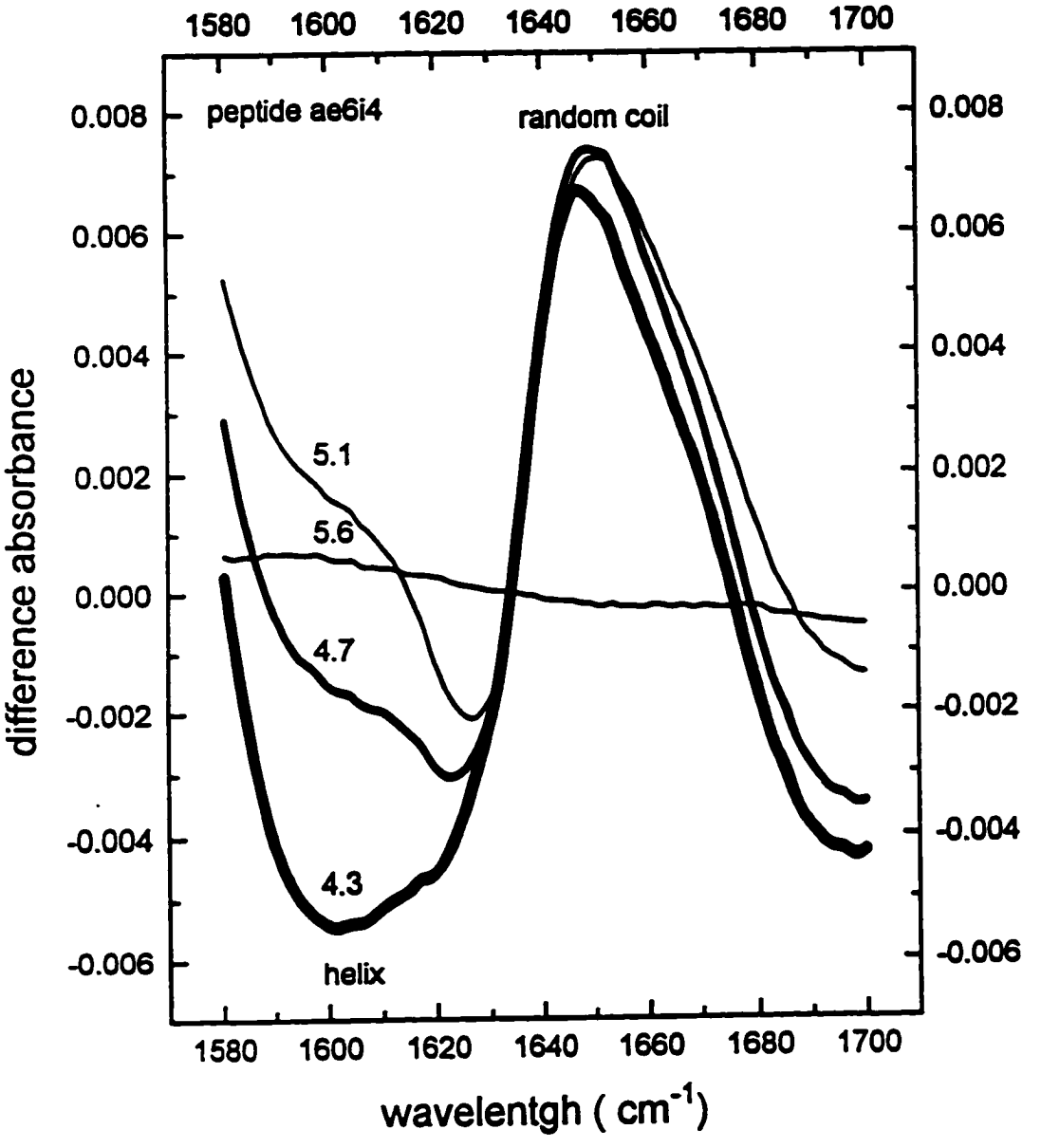

Fig. 5.7 Double differences spectra for peptide ae6i4 in the amide I region. The pH is indicated on each curve. The helical content increases with decreasing pH.

Reproduced with permission of the copyright owner. Further reproduction prohibited without permission.

BIBLIOGRAPHY

[1] K. Kawasaki, Ann. Phys. **61**, 1 (1970).

[2] E. Leutheusser, Phys. Rev. A **29**, 2765 (1984).

[3] U. Bengtzelius, W. Goetze and A. Sjolander, J. Phys. C **17** 5915 (1984).

[4] W. Petry et al., Z. Phys. B. **83**, 175 (1991).

[5] D. Richter, B. Frick, and B. Farago, Phys Rev. Lett. **61**, 2465 (1988).

[6] B. Frick, B. Farago and D. Richter, Phys. Rev. Lett. **64**, 2921 (1990).

[7] W. Knaak, F. Mezei and B. Farago, Europhys. Lett. **7**, 529 (1988).

[8] N.J. Tao, G. Li and H.Z. Cummins, Phys. Rev. Lett. **66**, 1334 (1991).

[9] G. Li , W.M. Du, X.K. Chen, H.Z. Cummins and N.J. Tao, Phys. Rev. A **45**, 3867 (1992).

[10] G. Li, W.M. Du, A Sakai, and H.Z. Cummins, Phys. Rev. A. **46**, 3343 (1992).

[11] W.M. Du, G. Li, H.Z. Cummins, M. Fuchs, J. Toulouse and L.A. Knauss, Phys. Rev. E **49**, 2192 (1994).

[12] H. Z. Cummins et al, Prog. Theor. Phys., suppl. no. 126 (1997) (in press).

[13] B. Berne and R. Pecora, Dynamic light scattering, Wiley-Interscience, New York (1976).

[14] D. Frenkel and J.P. McTague, J. Chem. Phys. **72**, 280 (1980).

[15] R. M. Lynden-Bell and K. H. Michel, Rev. Mod. Phys. **66**, 721 (1994).

[16] G.F. Signorini, J.L. Barrat and M.L. Klein, J. Chem. Phys. **92**, 1294 (1990).

[17] L. Silberstein, Philos. Mag. **33**, 521 (1917).

[18] M.J. Stephen, Phys. Rev. **187**, 279 (1969).

[19] H.Z. Cummins, G. Li, W. Du, R. M. Pick and C. Dreyfus, Phys. Rev. E **53**, 896 (1996). (erratum: Phys. Rev. E **55**, 1232 (1997)).

Reproduced with permission of the copyright owner. Further reproduction prohibited without permission.

[20] H. Z. Cummins and P. E. Schoen, in: Laser Handbook, edited by F. T. Arecchi and E. O. Schultz-Du Bois (North-Holland, Amsterdam 1971), p. 1029-1075.

[21] J. F. Nye, Physical Properties of Crystals (Oxford University Press, London, 1964). (For isotropic materials there are only two distinct Pockel's coefficients, p_{11} and p_{12}.) Also, typically for glass, p_{11}~0.12, p_{12} ~ 0.27, so that p_{11}/p_{12} ~ 0.45.

[22] M. Born and E. Wolf, Principles of Optics, 4th ed. (Pergamon, Oxford, 1970).

[23] C.A. Angel, J. Phys. Chem. Solids **49**, 863 (1988).

[24] P.K. Dixon, L. Wu, S.R. Nagel, B.D. Williams and J.P. Carini, Phys. Rev. Lett. **65**, 1108 (1990).

[25] N. Menon, K.P. O'Brien, P.K. Dixon, L. Wu, and S.R. Nagel, J. Non-Cryst. Solids **141**, 61 (1992).

[26] W. Goetze and L. Sjoegren, Rep. Prog. Phys. **55**, 241 (1992).

[27] W. Goetze, in Liquids, freezing and glass transition, edited by J.P. Hansen, D. Levesque and J. Zinn-Justin (North-Holland, Amsterdam, 1990), p. 287.

[28] J.P. Boon and S. Yip, Molecular Hydrodynamics, McGraw-Hill, New York (1980).

[29] U. Bengtzelius, Phys. Rev. A. **34**, 5059 (1986).

[30] W. Goetze and L. Sjoegren, J. Phys. C **21**, 3407 (1988).

[31] S.P. Das and G.F. Mazenko, Phys. Rev. A **34**, 2265 (1986).

[32] W. Goetze and L. Sjoegren, Z. Phys. B **65**, 415 (1987).

[33] W. Doster, S. Cusack and W. Petry, Phys. Rev. Lett. **65**, 1080 (1990).

[34] H.Z. Cummins et al., Phys. Rev. E **47**, 4223 (1993).

[35] J. Wuttke, J. Hernandez, G. Li, G. Coddens, H.Z. Cummins, F. Fujara, W. Petry, and H. Sillescu, Phys. Rev. Lett. **72**, 3052 (1994).

[36] H.Z. Cummins et al, Transport theory and statistical physics, **24**, 981 (1995).

[37] In fragile glass glasses T_c is generally ≈ 1.2 T_g [E. Rossler, Ber. Bunsenges. Phys. Chem. **94**, 392 (1990)].

Reproduced with permission of the copyright owner. Further reproduction prohibited without permission.

[38] L. Andrussow, in Landolt-Borstein, Vol. II, Pt. 5a (Springer, Berlin, 1969), 6th ed.

[39] About the same $T_c \approx 300K$ is found from $(\omega_{min})^{2a}$ with an exponent $a \approx 1$ as obtained from a free fit over the full high T scaling range.

[40] T. Franosch, W. Goetze, M. Mayr and A.P. Singh, Phys. Rev. E **55**, 3183 (1997).

[41] L. Sjoegren, Phys. Rev. A **33**, 1254 (1986).

[42] M. C. Tobin, Science **161**, 68-69 (1968).

[43] G. Burns and B. A. Scott, Phys. Rev. Lett. **25**, 1191-1194 (1970).

[44] W. J. Brya, Phys. Rev. Lett. **26**, 1114-1118 (1971).

[45] T. P. Martin and L. Genzel, Phys. Rev. B **8**, 1630-1635 (1973).

[46] G. M. Gualberto and C. A. Arguello, Solid State Comm. **14**, 911-914 (1974).

[47] J. A. McCammon, B. R. Gelin and M. Karplus, Nature **262**, 325-326 (1970).

[48] M. J. E. Sternberg, D. E. P. Grace and D. C. Philips, J. Mol. Biol. **130**, 231-253 (1979).

[49] G. Li, N. Tao, L. V. Hong, H. Z. Cummins, C. Dreyfus, M. Hebbache, R. M. Pick, and J. Vagner, Phys. Rev. B **42**, 4406-4425 (1990).

[50] R. Bechmann in Landolt-Borstein, new series, group III/vol. 2, p. 141, Springer-Verlag, Berlin (1969).

[51] L. J. Bellamy, The infrared spectra of complex molecules, 2nd ed., vol. 2, p.176 (Chapman and Hall, New York, 1980).

Reproduced with permission of the copyright owner. Further reproduction prohibited without permission.